molecules

MDPI

Article

Ag-Doped CaO/ZnO Nanocomposite from Eggshell Waste: Mechanistic Insights into Rhodamine B Photodegradation Under UV and Visible Light

Seloua Khalfoun [1], Youcef Sedkaoui [1], Gianluca Viscusi [2], Feras Mohammed Afifi [3], Tarek H. Taha [4], Hamdi Bendif [4,*] and Lotfi Mouni [5,*]

[1] Laboratoire des Matériaux et Développement Durable (LMDD), Faculty of Applied Sciences, University of Bouira, Bouira 10000, Algeria; y.sedkaoui@univ-bouira.dz (Y.S.)
[2] Department of Industrial Engineering, University of Salerno, 84084 Fisciano, Italy
[3] Physics Department Al-Leith University College, Umm Al-Qura University, Makkah 24382, Saudi Arabia
[4] Biology Department, College of Science, Imam Mohammad Ibn Saud Islamic University (IMSIU), Riyadh 11623, Saudi Arabia
[5] Laboratoire de Gestion et Valorisation des Ressources Naturelles et Assurance Qualité, Faculté SNVST, Université de Bouira, Bouira 10000, Algeria
* Correspondence: hlbendif@imamu.edu.sa (H.B.); l.mouni@univ-bouira.dz (L.M.)

Abstract

In this study, we report an eco-friendly route for synthesizing calcium oxide (CaO) and a CaO/ZnO/Ag heterostructure to assess their performance in the photocatalytic degradation of Rhodamine B (RhB). CaO was recovered from chicken eggshell waste through optimized calcination, while the CaO/ZnO/Ag composite was prepared via green solution co-precipitation followed by thermal treatment at 400 °C for 2 h. Characterization by XRD, FTIR, FESEM/EDX, BET, and UV-Vis spectroscopy confirmed the successful formation of the targeted composite, with a mesoporous architecture (14.88 m^2/g, 23.70 nm pore diameter) and a narrowed bandgap of 2.92 eV (vs. 3.15 eV for pristine ZnO). The CaO/ZnO/Ag nanocomposite achieved RhB removal within 9 min under UV-A irradiation and within 35 min under artificial visible light with H_2O_2, substantially outperforming individual CaO and ZnO. Under natural sunlight with H_2O_2, degradation was reached in 20 min. Radical scavenging revealed condition-dependent mechanisms: •OH and h^+ dominated under UV, whereas $•O_2^-$ and •OH prevailed under visible light/H_2O_2. The catalyst retained 85.62% activity after nine UV cycles but only 60.66% after five visible-light/H_2O_2 cycles. These findings demonstrate the potential of eggshell-derived CaO/ZnO/Ag as an efficient, durable, and sustainable photocatalyst for dye-contaminated wastewater, offering an effective waste-to-value strategy for converting biogenic waste into advanced environmental materials.

Keywords: eggshell waste; Rhodamine B; photocatalysis; Ag-doped CaO/ZnO nanocomposite

Check for updates

Academic Editors: Lucyna Bilińska and Yongchang Sun

Received: 26 October 2026
Revised: 10 November 2026
Accepted: 12 November 2026
Published: 16 November 2026

Copyright: © 2026 by the authors. Licensee MDPI, Basel, Switzerland. This article is an open access article distributed under the terms and conditions of the Creative Commons Attribution (CC BY) license.

1. Introduction

Water pollution has become increasingly difficult to manage because rapid industrialization, urban expansion, and growing water demand are placing additional pressure on freshwater resources. Industrial effluents frequently contain persistent organic pollutants that are poorly removed by conventional biological and physicochemical treatment processes. These limitations include incomplete degradation, high chemical and energy

requirements, and the formation of secondary residues or sludge, thereby encouraging the development of more efficient and sustainable treatment technologies [1].

Synthetic dyes are among the most problematic industrial contaminants because of their chemical stability, intense coloration, high water solubility, and resistance to biodegradation. Rhodamine B (RhB), a xanthene dye widely used in textile, paper-printing, leather, and laboratory applications, is frequently employed as a model pollutant for evaluating advanced water-treatment technologies. Its persistent aromatic structure and toxicological concerns make its effective removal from contaminated water particularly important [2,3]. Conventional processes, including adsorption, coagulation, membrane filtration, and biological treatment, may reduce dye concentration or color but do not always ensure complete chemical degradation or eliminate potentially harmful transformation products [4,5].

Advanced oxidation processes (AOPs), particularly heterogeneous photocatalysis, have therefore attracted considerable attention for the treatment of dye-contaminated wastewater. These processes rely on the formation of highly reactive species, including hydroxyl radicals, superoxide radicals, photogenerated holes, and other reactive oxygen species, which can attack chromophoric groups and aromatic structures [6]. Photocatalysis has emerged as an attractive AOP due to its low cost, environmental benignity, strong oxidative capability, high mineralization efficiency, and operational ease [7]. It has been regarded as a powerful tool in the fight against bacterial diseases and water pollution [8,9]. The efficiency of photocatalytic degradation depends on several interacting parameters, including catalyst composition, surface properties, pH, pollutant concentration, catalyst dosage, oxidant concentration, and irradiation wavelength [10]. However, the practical application of photocatalysis still requires catalysts that combine high activity with low-cost synthesis, efficient light utilization, easy recovery, and long-term stability [11,12].

Zinc oxide is a promising semiconductor for photocatalytic applications because of its high chemical stability, strong redox capacity, and suitable optical properties. Nevertheless, its wide bandgap, approximately 3.3–3.4 eV, restricts its intrinsic activity mainly to the ultraviolet region and favors the recombination of photogenerated electron–hole pairs. Incorporating silver into ZnO can improve the photocatalytic response through metal–semiconductor interactions, electron-trapping effects, and localized surface plasmon resonance. These effects can enhance light absorption, facilitate charge separation, and increase the lifetime of the charge carriers involved in surface redox reactions [13,14]. Recent Ag/ZnO-based photocatalysts have demonstrated improved dye degradation under visible or solar irradiation, confirming the potential of plasmonic silver modification for environmental remediation [15,16].

The use of agricultural and food-processing wastes as precursors for functional materials provides an additional strategy for reducing the environmental and economic impacts associated with nanomaterial production [17,18]. Chicken eggshells are particularly attractive because their mineral fraction consists predominantly of calcium carbonate, which can be converted into calcium oxide through thermal treatment. Eggshell-derived CaO has been investigated as a low-cost material for catalytic and environmental applications, and its basic surface properties can promote interactions with organic pollutants while contributing to the development of composite photocatalysts [19]. Waste-derived calcium-based materials and metal-oxide hybrids have attracted growing interest for pollutant removal, as they combine low-cost resource recovery with the principles of the circular economy [20,21].

Combining eggshell-derived CaO with ZnO and Ag offers a promising route for designing a multifunctional photocatalyst. In such a system, CaO can contribute basic surface sites and influence the surface chemistry and morphology of the composite, while ZnO can provide semiconductor photocatalytic activity, and Ag can promote interfacial charge transfer and visible-light absorption. The resulting composite may therefore combine the

adsorptive and catalytic properties of CaO with the improved charge-separation characteristics of Ag-modified ZnO. This design concept is consistent with recent reports showing that Ag-containing ZnO heterostructures can improve light absorption, suppress charge recombination, and promote the formation of reactive oxygen species during dye degradation [14,22].

In the present study, eggshell-derived CaO was prepared by calcination at 900 °C for different treatment durations, namely 30 min, 1 h, 2 h, and 4 h, to determine the most suitable preparation condition. The optimized CaO was subsequently integrated with ZnO and Ag through a co-precipitation route followed by thermal treatment. The structural, chemical, morphological, elemental, textural, and optical properties of the synthesized materials were investigated using X-ray diffraction, Fourier-transform infrared spectroscopy, field-emission scanning electron microscopy coupled with energy-dispersive X-ray spectroscopy, Brunauer–Emmett–Teller analysis, and UV–Vis spectroscopy. The photocatalytic performance of the Ag-doped CaO/ZnO nanocomposite was evaluated using RhB as a model pollutant under UV-A irradiation, artificial visible light, and natural sunlight. The study also examined the influence of operational parameters, the contribution of reactive species through scavenger experiments, and the reusability of the photocatalyst. This work establishes a waste-valorization strategy for producing a low-cost and multifunctional photocatalyst for dye-contaminated wastewater treatment.

2. Results and Discussion

2.1. ATR-FTIR Analysis

The ATR-FTIR spectra of the eggshell-derived CaO samples calcined at different holding times (30 min, 1 h, 2 h, and 4 h) are illustrated in Figure 1a. All spectra exhibit characteristic absorption bands confirming the successful thermal conversion of the biogenic calcium carbonate precursor into calcium oxide (CaO). The prominent and sharp stretching vibration band observed around 3641 cm^{-1} corresponds to the O–H stretching mode of surface-adsorbed hydroxyl groups or trace calcium hydroxide ($Ca(OH)_2$), formed due to the slight hydration of active CaO upon brief ambient exposure [23–25]. The strong, broad absorption band centered around 1414 cm^{-1} is attributed to the asymmetric stretching vibrations of carbonate (CO_3^{2-}) groups, originating from minor surface carbonation resulting from atmospheric CO_2 adsorption [25]. Furthermore, the sharp band observed near 874 cm^{-1} corresponds to the out-of-plane bending vibration of the carbonate group, while the intense absorption bands appearing at 548 and 440 cm^{-1} are characteristic of the metal–oxygen (Ca-O) stretching vibrations, confirming the formation of the crystalline CaO lattice [26]. Notably, spectra across all calcination durations (30 min to 4 h) display nearly identical profiles, indicating that phase transformation and structural stabilization are rapidly achieved, yielding high-purity CaO regardless of extended holding times [27]. Figure 1b compares the FTIR transmission spectra of pristine ZnO, Ag-doped ZnO, and the Ag-doped CaO/ZnO nanocomposite, demonstrating distinct structural modifications and successful phase integration. The pristine ZnO spectrum exhibits several absorption bands in the low-wavenumber region, particularly near 419, 499, and 559 cm^{-1}. These bands are associated with Zn-O lattice vibrations and confirm the formation of the ZnO phase [28,29]. The band located at approximately 504 cm^{-1} in the Ag-modified ZnO sample confirms the preservation of the Zn-O framework after silver incorporation. The slight displacement and variation in the intensity of this band suggest a modification of the local coordination environment and the introduction of lattice distortion or defect sites associated with Ag incorporation. Similar FTIR and structural changes have been reported for Ag-containing ZnO nanomaterials, in which silver incorporation modifies the ZnO lattice while preserving its wurtzite structure [30–32].

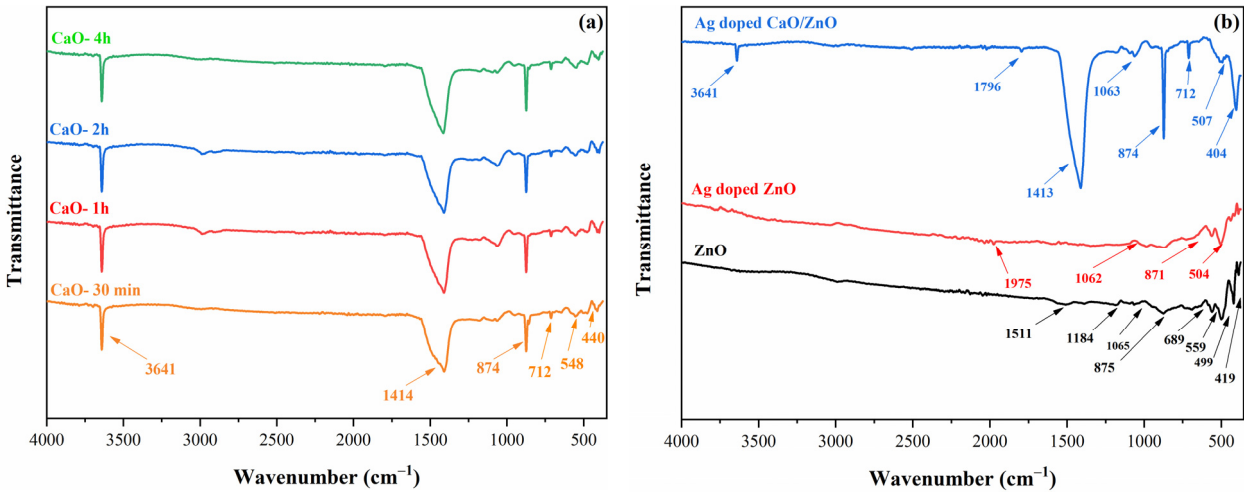

Figure 1. ATR-FTIR spectra of: (**a**) eggshell-derived CaO nanoparticles synthesized at different calcination holding times (30 min, 1 h, 2 h, and 4 h); (**b**) comparative spectra of pure ZnO, Ag-doped ZnO, and Ag-doped CaO/ZnO nanocomposite samples.

Notably, the spectrum of the Ag-doped CaO/ZnO nanocomposite displays low-frequency bands at approximately 404 and 507 cm^{-1}. These absorptions are assigned to overlapping metal–oxygen lattice vibrations involving Zn-O and Ca-O bonds. The assignment is supported by comparison with the individual oxide phases, in which ZnO typically exhibits Zn-O vibrations in the lower wavenumber region, while eggshell-derived CaO displays Ca-O-related bands in a similar spectral region. The overlap and slight displacement of these bands in the composite suggest the coexistence of the CaO and ZnO phases, with possible local changes in the metal–oxygen environment after Ag incorporation [19]. A sharp, intense absorption band around 1413 cm^{-1} accompanied by a sharp band near 871 cm^{-1} is assigned respectively to asymmetric stretching and out-of-plane bending of carbonate species originating from minor surface carbonation due to atmospheric CO_2 adsorption [25].

2.2. XRD Structural Characterization

Figure 2a presents the X-ray diffraction patterns of the eggshell-derived CaO samples calcined at 900 °C for different holding times. The diffraction profiles show reflections characteristic of crystalline calcium oxide with a face-centered cubic structure (Fm3m space group). The main peaks, located at 2θ = 32.20°, 37.45°, 54.00°, 64.33°, 67.56°, and 79.89°, are indexed to the (111), (200), (220), (222), (311), and (400) planes of CaO, respectively. These reflections match the reference pattern for cubic CaO (JCPDS card No. 37-1497), confirming successful conversion of the eggshell-derived calcium carbonate precursor into CaO. The lattice parameter was calculated to be approximately a = 4.7990 Å, consistent with reported values for cubic CaO. No additional intense reflections were detected, indicating that CaO is the predominant crystalline phase in all samples.

The average crystallite size was estimated using the Debye–Scherrer equation (Equation (1)):

$$D = \frac{K\lambda}{\beta\cos\theta} \quad (1)$$

where D is the mean crystallite size, K is the shape factor (taken as 0.90), λ is the wavelength of Cu Kα radiation (1.5406 Å), β is the full width at half maximum of the diffraction peak (in radians), and θ is the corresponding Bragg angle. The resulting average crystallite sizes were 49.57, 50.41, 50.44, and 51.80 nm for the samples calcined for 30 min, 1 h, 2 h, and 4 h, respectively. This gradual increase in crystallite size with longer holding times

suggests that extended calcination favors crystal growth and particle coalescence. The diffraction pattern of pristine ZnO shows the reflections typical of hexagonal wurtzite ZnO, particularly near 2θ = 31.7°, 34.4°, and 36.2°, corresponding to the (100), (002), and (101) planes, in agreement with the ZnO reference pattern (JCPDS No. 36-1451). The pattern of Ag-doped ZnO/CaO retains the principal ZnO reflections while showing additional peaks attributable to the CaO phase, consistent with the CaO reference pattern (JCPDS No. 37-1497). Following Ag incorporation, the dominant ZnO reflections are preserved, indicating that the wurtzite structure remains intact. No clearly resolved peaks corresponding to face-centered cubic silver were expected near 38.1°, 44.3°, 64.4°, and 77.5° for the (111), (200), (220), and (311) planes were observed in either the Ag-doped ZnO or the Ag-doped ZnO/CaO composite. The absence of distinct Ag reflections does not necessarily indicate the absence of silver, since XRD mainly detects crystalline phases with sufficient long-range order and concentration. At low Ag loading, silver may be highly dispersed on the ZnO surface, located at grain boundaries, present in very small crystallites, or below the detection limit of the diffractometer. Under these conditions, Ag scattering can be weak or broad and easily masked by the more intense ZnO reflections and, in the ternary composite, by the additional CaO signal [32,33]. The average crystallite sizes derived from the XRD patterns were 59.06 nm for pristine ZnO, 57.90 nm for Ag-doped ZnO, and 57.19 nm for the Ag-doped CaO/ZnO composite. Relative to pristine ZnO, Ag incorporation led to a modest decrease of 1.16 nm (~2.0%), while the further addition of CaO resulted in a total reduction of 1.87 nm (~3.2%). The difference between the Ag-doped ZnO and Ag-doped CaO/ZnO samples was only 0.71 nm, suggesting that Ag and CaO incorporation produced a slight grain-refinement effect without substantially altering the underlying ZnO crystalline framework.

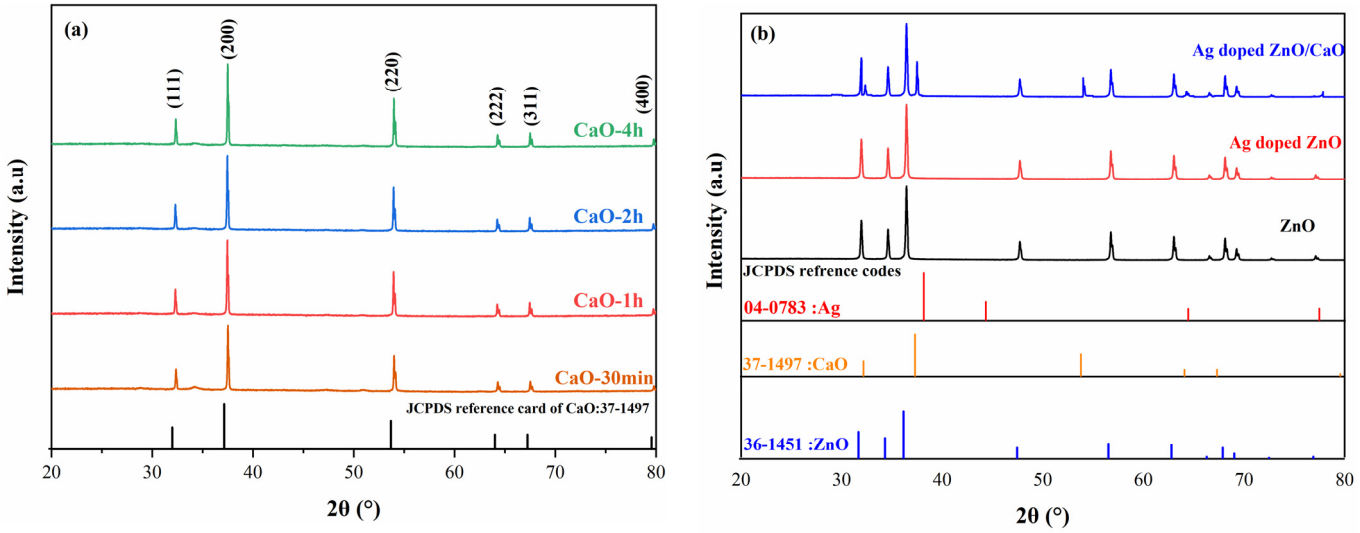

Figure 2. XRD patterns of: (**a**) CaO samples obtained at 900 °C for different calcination times (30 min, 1 h, 2 h, and 4 h); (**b**) pristine ZnO, Ag-doped ZnO, and Ag-doped ZnO/CaO composite.

2.3. SEM and EDX Analysis

The surface morphology of the synthesized CaO nanoparticles was examined by scanning electron microscopy (SEM), as shown in Figure 3a–d. The micrographs reveal a well-defined, hierarchical flower-like architecture, formed by interconnected primary crystallites aggregated into cauliflower-like clusters that impart a highly textured, three-dimensional surface. Comparative SEM analysis of the samples calcined at 900 °C for 30 min, 1 h, 2 h, and 4 h showed no significant morphological changes with increasing holding time, indicating that microstructural development was essentially complete within the first 30 min of thermal treatment. These findings confirm that a short calcination period

at 900 °C is sufficient to achieve the target morphology, offering a route to reduce both energy consumption and processing time without compromising the structural quality of the resulting CaO precursors. EDX analysis confirmed the formation of pure CaO across all calcination durations tested (30 min, 1 h, 2 h, and 4 h), demonstrating that calcining eggshells at 900 °C for as little as 30 min is enough to achieve complete $CaCO_3$ decomposition and yield phase-pure CaO nanoparticles, with an elemental composition of 43.77 wt% Ca and 46.43 wt% O. SEM analysis of the samples calcined at 400 °C for 2 h (Figure 3e–g) reveals a progressive change in morphology. Pure ZnO predominantly displays a nanorod structure, while Ag incorporation drives a shift toward nanoplatelet formation. This transition is further enhanced in the Ag-doped CaO/ZnO sample, which exhibits well-defined, porous nanoplatelets with rigid, faceted geometries. These planar structures undergo random self-assembly, driven by interparticle van der Waals forces and electrostatic interactions at the nanoscale, leading to three-dimensionally stacked aggregates with increased inter-platelet porosity. The corresponding FESEM/EDX images in Figure 3 confirm that the nanocomposites consist of two-dimensional porous nanoplates with a rigid, angular central structure. Under nanoscale surface attraction forces, these nanoplates self-assemble and stack irregularly to form three-dimensional clusters. The EDX spectra display characteristic signals for Zn, Ag, Ca, and O, confirming the elemental composition of the synthesized nanocomposites. A minor carbon (C) signal is detected across all spectra, most likely originating from the conductive carbon tape used to mount the powdered samples on the SEM stub, rather than reflecting the structural composition of the material [34].

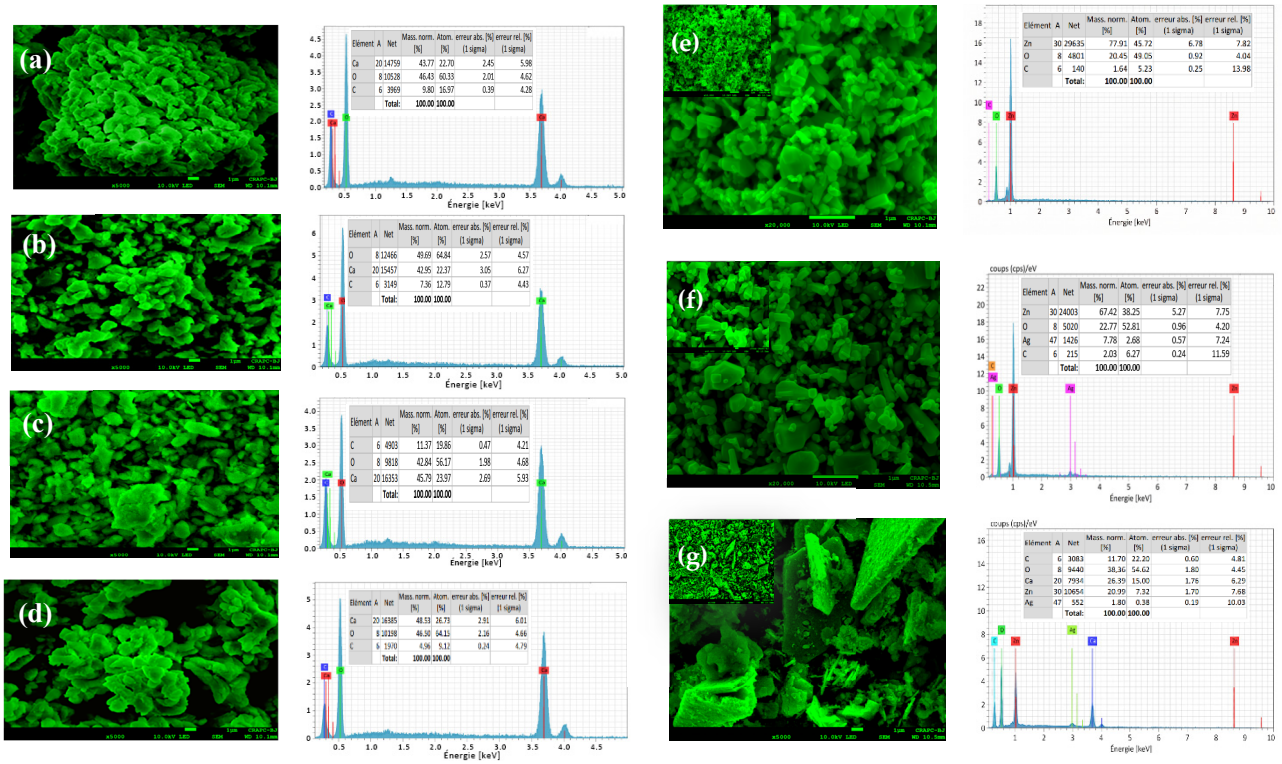

Figure 3. FESEM micrographs showing morphological evolution, with corresponding EDX spectra, for: (**a**–**d**) CaO samples calcined at 900 °C for varying soaking times; and (**e**–**g**) pure ZnO nanorods, Ag-doped ZnO nanoplatelets, and the porous Ag-doped CaO/ZnO nanocomposite.

2.4. BET Analysis

The textural properties of the different CaO samples were assessed by nitrogen adsorption–desorption (BET) analysis and correlated with their corresponding average particle sizes (Figure 4). A typical inverse relationship between specific surface area (SBET)

and average particle diameter (Dp) was observed, whereby smaller particle sizes correspond to proportionally higher surface areas [35]. Comparing commercial CaO with the eggshell-derived samples highlights the structural benefits of the biogenic precursor: commercial CaO showed a relatively low surface area of 5.71 m^2/g, corresponding to a micrometric particle size of 1051.60 nm, whereas CaO obtained from waste eggshells after just 30 min of calcination at 900 °C exhibited a considerably higher surface area of 9.26 m^2/g and a smaller particle size of 647.92 nm. This enhancement is attributed to the porous structure and inherent organic matrix of the eggshell, which acts as a natural template during thermal decomposition, limiting the extensive particle coalescence and sintering typically observed during industrial processing of geological limestone precursors [35,36]. Extending the calcination time from 30 min to 4 h at 900 °C further refined the microstructure considerably: the specific surface area rose by roughly 68%, from 9.26 to 15.57 m^2/g, while the particle size decreased substantially from 647.92 to 385.26 nm. Since complete decarbonation of $CaCO_3$ into CaO occurs within the first 30 min, as verified by EDX and SEM analyses, this ongoing microstructural change is primarily physical rather than chemical in nature [37]. At 30 min, the newly formed CaO particles exist as large, loosely packed agglomerates expanded by the rapid release of CO_2 during decomposition [38]. Prolonged heating is thought to promote the progressive fragmentation of these agglomerates and the development of additional porosity, exposing more surface area [37]. This trend is notable, since extended heating at 900 °C would normally be expected to cause sintering and a loss of surface area [39].

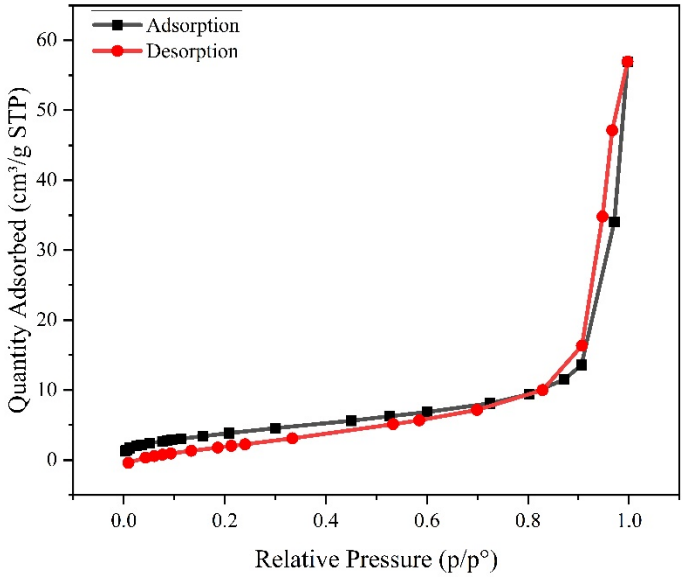

Figure 4. BET analysis showing nitrogen adsorption–desorption isotherm and pore size distribution of the synthesized Ag-doped CaO/ZnO nanocomposite.

BET analysis was also used to examine the textural characteristics and porosity of the synthesized Ag-doped CaO/ZnO nanocomposite (Table 1 and Figure 4). The nitrogen adsorption–desorption isotherm displays Type IV behavior with a distinct hysteresis loop, confirming a well-developed mesoporous structure and multilayer adsorption. The material showed a specific surface area of 14.88 m^2/g, a total pore volume of 0.088148 cm^3/g, and an average pore diameter of 23.70 nm.

This predominantly mesoporous structure offers abundant accessible active sites and efficient mass-transfer pathways, contributing to enhanced catalytic performance [40].

Table 1. BET analysis results of synthesized Ag-doped CaO/ZnO nanocomposite.

Surface Area (m^2/g)	Total Pore Volume (cm^3/g)	Adsorption Average Pore (nm)	BJH Adsorption Average Pore Diameter (nm)	BJH Desorption Average Pore Diameter (nm)
14.8763	0.088148	23.70	21.58	18.32

2.5. Optical Properties

The optical band gap energy (Eg) of the synthesized CaO nanoparticles was calculated from UV–Vis diffuse reflectance spectroscopy (DRS) using the Tauc method [41]. The calculated values for eggshell-derived CaO calcined at 900 °C for different durations are summarized in Figure 5a. All samples displayed wide band gap energies between 5.74 and 5.81 eV, in line with the intrinsic optical behavior of calcium oxide as a wide-bandgap semiconductor [42,43]. The samples calcined for 30 min and 2 h shared an identical value of 5.78 eV; the 1 h sample showed a slightly higher value of 5.81 eV, and a marginal decrease to 5.74 eV was observed after 4 h. This nearly constant Eg across calcination times suggests that the electronic structure of CaO is established within the first 30 min of thermal treatment, consistent with the completion of $CaCO_3$ decomposition confirmed by EDX and XRD. The small decrease at 4 h (≈0.04 eV) is within the typical uncertainty of the Tauc analysis and may be related to improved crystallinity and a lower density of structural defects or residual carbonate species resulting from extended heating [44]. Since the particle sizes (≈385–648 nm) are far above the quantum-confinement regime, no size-dependent effect on Eg is expected. Because the 30 min calcination produces essentially the same band gap (5.78 eV) as longer treatments while offering clear benefits in energy efficiency and processing time, this duration represents the best compromise between optical quality and operational cost. Moreover, extended calcination at high temperature risks sintering-induced degradation, which can negatively affect the textural properties needed for practical applications. A calcination time of 30 min at 900 °C is therefore identified as the optimal condition for obtaining CaO precursors with well-defined optical characteristics [35].

The optical properties of pristine ZnO, the binary Ag-doped ZnO composite, and the ternary Ag-doped CaO/ZnO nanocomposite were analyzed by UV–Vis DRS combined with Tauc plots [$(\alpha h\nu)2$ vs. $h\nu$], with the UV–Vis spectra provided in Figure 5c,d. Pristine ZnO showed a direct band gap of approximately 3.15 eV. For the Ag-containing samples, the values obtained are apparent band gaps, i.e., absorption-edge energies of the ZnO phase in a multiphase material, and not intrinsic band gaps of the composites. A slight decrease to 3.09 eV was observed for Ag/ZnO, which may be related to Ag-induced defect-related states near the band edge while the wurtzite lattice is preserved [45]. In addition, the localized surface plasmon resonance (LSPR) of Ag nanoparticles contributes to extra absorption in the visible region, without modifying the band gap of ZnO itself. In the ternary CaO/ZnO/Ag system, the apparent band gap decreased further to 2.92 eV. This red shift in the absorption edge is attributed to interfacial and defect-related states at the CaO/ZnO and Ag/ZnO interfaces, together with Ag-related absorption, which extend the absorption toward lower energies [46]. The grain restructuring observed by SEM may also contribute through increased structural disorder.

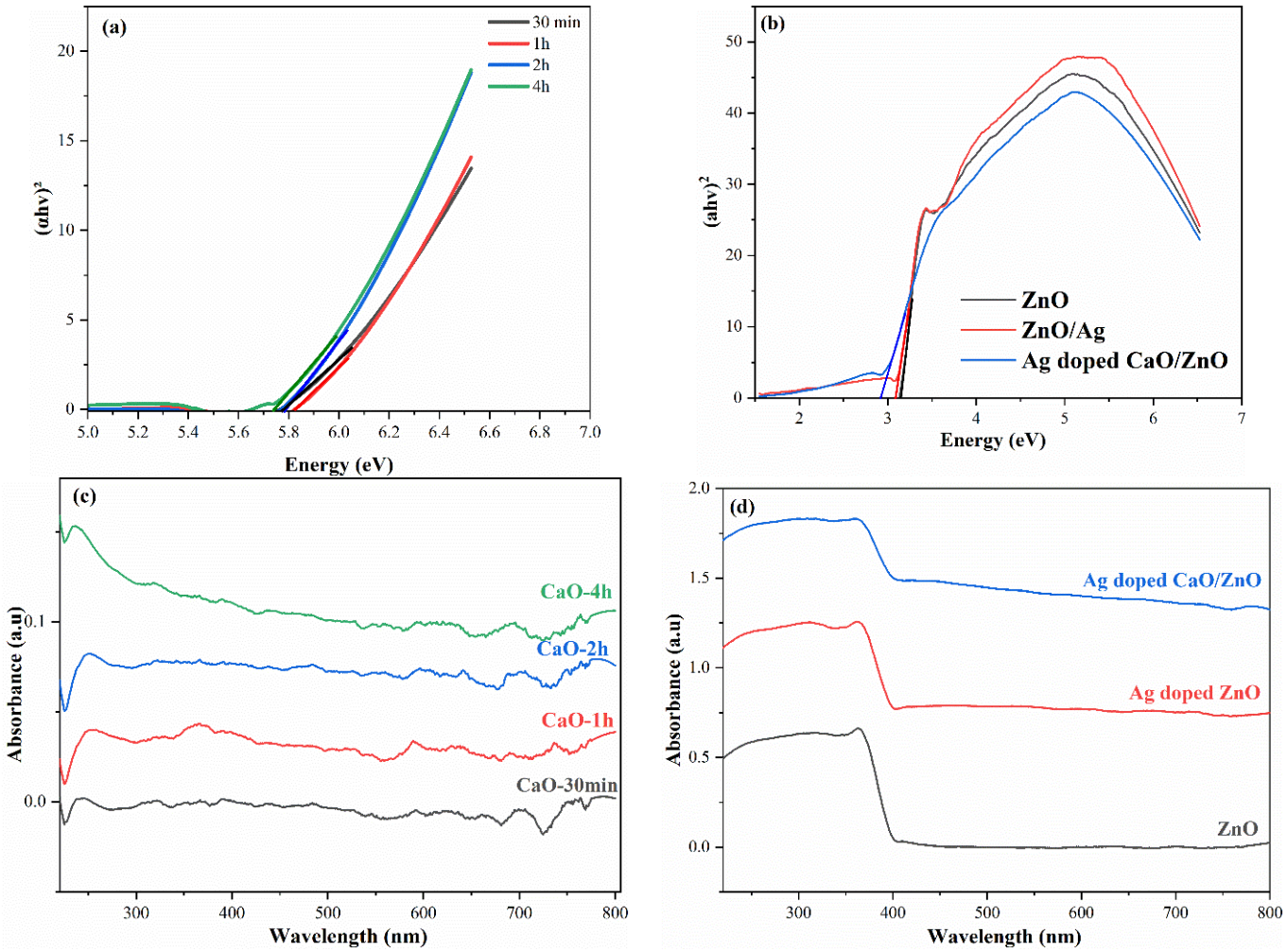

Figure 5. Tauc plots for estimating the optical band gaps of (**a**) eggshell-derived CaO calcined at 900 °C for different durations and (**b**) ZnO, Ag-doped ZnO, and Ag-doped CaO/ZnO. (**c**,**d**) Corresponding UV–Vis absorbance spectra.

2.6. Point of Zero Charge (pH_{zpc})

The point of zero charge (pHzpc) of the Ag-doped CaO/ZnO nanocomposite, determined by the pH drift method (0.1% NaCl, pH 2–11, 48 h equilibration), was found to be 10.66 (Figure 6). This parameter is critical for interpreting photocatalytic behavior, as it defines the pH-dependent surface charge governing electrostatic interactions with the target pollutant: below pHzpc, protonation renders the surface positively charged, favoring adsorption of anionic species, while above pHzpc, deprotonation produces a negatively charged surface favoring cationic-dye interaction [47]. Since pollutant adsorption onto active surface sites is a prerequisite for efficient charge-transfer and radical-mediated degradation, a high pHzpc such as 10.66 indicates that the catalyst surface remains positively charged over a wide pH range, favoring electrostatic attraction toward anionic pollutants [45].

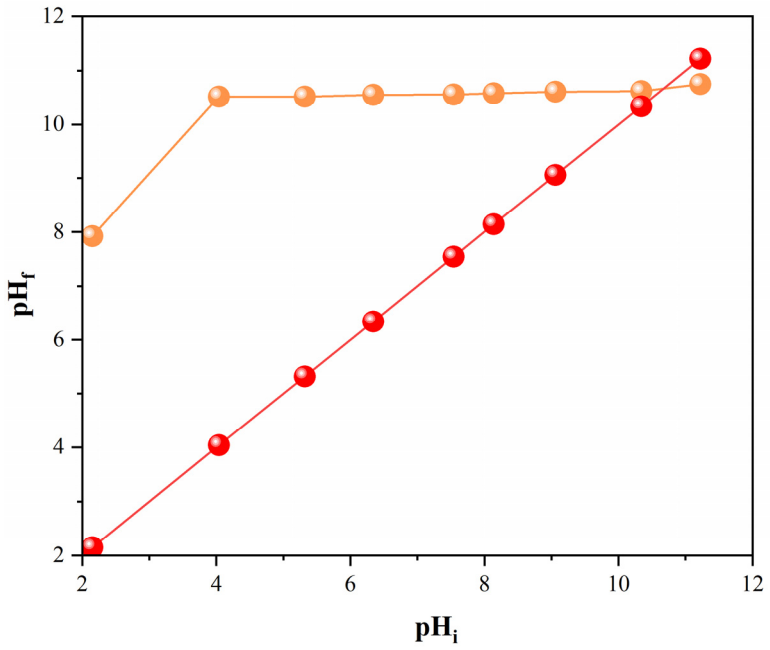

Figure 6. Determination of the point of zero charge (pH_{pzc}) of the Ag-doped CaO/ZnO composite by the pH drift method.

3. Materials and Methods

All chemical reagents used in this study were of analytical grade and employed without further purification. Zinc nitrate hexahydrate ($Zn(NO_3)_2{\cdot}6H_2O$, ≥98%) and silver nitrate ($AgNO_3$, ≥99%) were procured from Sigma-Aldrich (Steinheim, Germany). Rhodamine B (RhB, $C_{28}H_{31}ClN_2O_3$, M = 479.01 g/mol, purity ≥ 95%) was obtained from Biochem (Cosne-Cours-sur-Loire, France). Eggshells were collected from domestic kitchen waste and used as the calcium oxide precursor. Deionized water was used throughout all experimental procedures and washing steps.

3.1. Synthesis of Calcium Oxide Nanoparticles (CaO NPs)

Waste eggshells were collected from domestic sources and rinsed repeatedly with tap water to remove the inner membrane and any residual organic matter. The cleaned shells were then dried overnight in a hot-air oven at 80–100 °C. Following complete drying, the brittle shells were pulverized into a fine, pale-yellow powder using an electric grinder. A precisely measured mass of the eggshell powder, predominantly composed of calcium carbonate ($CaCO_3$), was transferred to a ceramic crucible and subjected to calcination in a muffle furnace at a fixed temperature of 900 °C under atmospheric conditions. To investigate the effect of calcination duration on the structural and morphological characteristics of the resulting nanoparticles, the thermal treatment was performed for varying time intervals of 30 min, 1 h, 2 h, and 4 h. The as-obtained samples were designated as CaO-900(30), CaO-900(1), CaO-900(2), and CaO-900(4), where the numbers in parentheses represent the calcination time (30 in minutes and 1, 2, and 4 in hours). Upon completion of the thermal decomposition, the conversion of $CaCO_3$ to CaO (Equation (2)) was evidenced by the formation of a characteristic white powder, signifying complete decarbonation through the release of CO_2 [48].

$$CaCO_3(s) \xrightarrow{\Delta} CaO(s) + CO_2(g) \quad (2)$$

3.2. Synthesis of Ag-Doped ZnO/CaO Nanocomposites

The Ag-doped ZnO/CaO nanocomposite powders (NCPs), formulated with a nominal composition of 60 wt% CaO, 35 wt% ZnO, and 5 wt% Ag, were prepared through a green co-precipitation route employing zinc nitrate hexahydrate ($Zn(NO_3)_2{\cdot}6H_2O$), silver nitrate ($AgNO_3$), and eggshell-derived calcium oxide (CaO) as starting precursors. In a typical procedure, a predetermined quantity of $Zn(NO_3)_2{\cdot}6H_2O$ was dissolved in 50 mL of deionized (DI) water under constant magnetic stirring at ambient temperature (25 °C). Separately, high-purity CaO powder was obtained through the calcination of cleaned eggshell waste at 900 °C for 30 min in a muffle furnace (Figure 7). The as-obtained CaO powder was then gradually added to the zinc precursor solution, weighed according to the targeted 60:35 CaO:ZnO ratio, under sustained stirring until the formation of a homogeneous white precipitate was observed. The addition of CaO served a dual function: it provided the calcium oxide component of the composite and simultaneously elevated the solution pH to approximately 12, thereby facilitating the precipitation of ZnO within minutes. Notably, this approach eliminates the requirement for conventional strong bases such as sodium hydroxide (NaOH), thereby adhering to the principles of green chemistry. The resulting suspension was aged under continuous stirring for 10 min to ensure complete precipitation. Subsequently, 20 mL of an aqueous $AgNO_3$ solution (0.023 M; 0.0787 g of $AgNO_3$) was introduced into the suspension and kept under stirring for an additional 50 min to promote uniform silver incorporation within the CaO/ZnO matrix. The $AgNO_3$ amount was calculated to give a nominal composition of 60 wt% CaO, 35 wt% ZnO, and 5 wt% Ag in the final nanocomposite. Following the precipitation step, the collected product was subjected to sequential washing with DI water until the supernatant reached neutral pH, thereby removing residual ionic species and unreacted precursors. The washed precipitate was dried in a forced-air oven at 80 °C for 2 h and subsequently calcined at 400 °C for 2 h under ambient atmosphere to yield the final gray-colored nanocomposite powders.

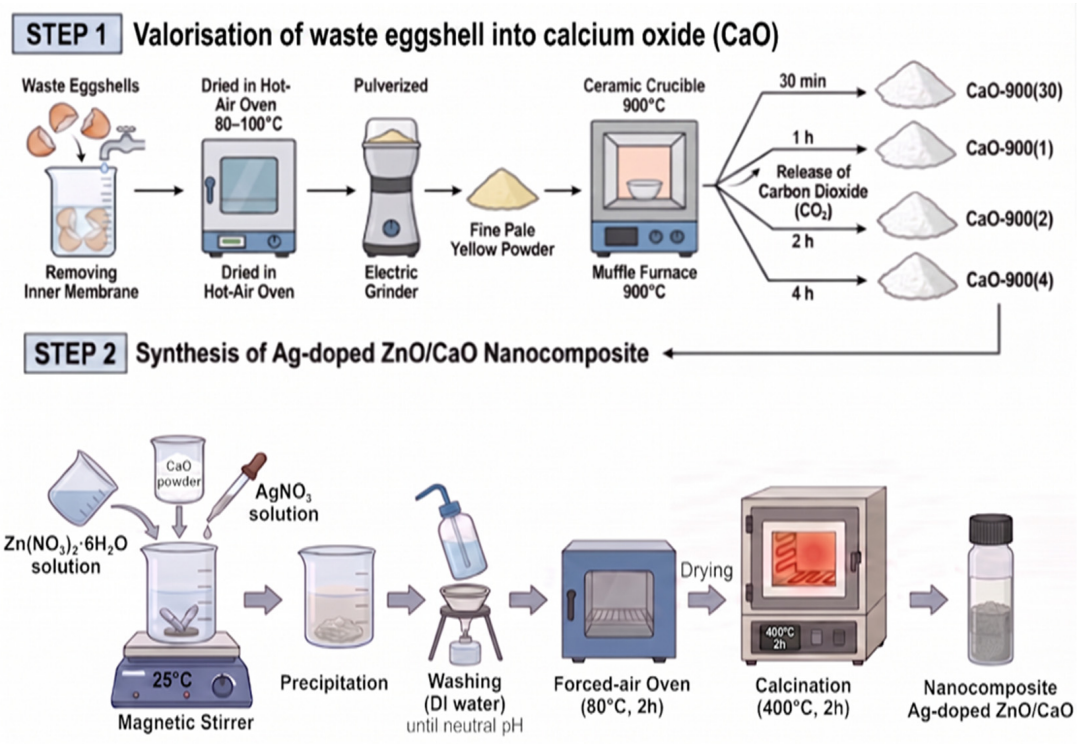

Figure 7. Synthesis of Waste Eggshell-Derived CaO and Ag-Doped ZnO/CaO Nanocomposites.

3.3. Photocatalytic Tests

Photodegradation experiments were performed in reaction vessels containing 50 mL of aqueous RhB solution (10 mg/L) and 80 mg of the corresponding photocatalyst. Prior to irradiation, the suspensions were magnetically stirred in the dark for 40 min to establish adsorption–desorption equilibrium between the dye molecules and the catalyst surface, with equilibrium generally attained within 10 min.

The suspensions were irradiated with natural sunlight (117.7 klux), a 42 W visible LED lamp ($\lambda = 450$ nm), and a 48 W UVA lamp ($\lambda = 365$ nm), with the lamp-to-reactor distance fixed at 22 cm. The effect of solution pH was examined over the range of 3–11, adjusted using 0.1 M HCl and 0.1 M NaOH solutions. In addition, the influence of oxidant supplementation was investigated by introducing varying volumes (5–80 µL) of hydrogen peroxide (H_2O_2, 30% *w*/*w*) into the reaction system while keeping the catalyst dosage and reaction volume constant, and the suspension was stirred at 200 rpm.

Reaction kinetics were monitored by withdrawing aliquots at fixed time intervals of 1 min for the UV- and solar-driven systems in the absence of H_2O_2, and every 5 min for the visible-light and H_2O_2 assisted solar systems. The withdrawn aliquots were centrifuged to remove the solid catalyst, and the residual RhB concentration in the supernatant was determined spectrophotometrically at its characteristic absorption maximum ($\lambda_{max} = 554$ nm). The photocatalytic degradation efficiency, D (%), was calculated as in Equation (3):

$$D(\%) = \frac{C_0 - C_t}{C_0} * 100 \quad (3)$$

where C_0 denotes the equilibrium RhB concentration following dark adsorption, and C_t represents the residual dye concentration at irradiation time t.

The photodegradation kinetics were further evaluated using the Langmuir–Hinshelwood pseudo-first-order kinetic model (Equation (4)) [49]:

$$r = -\frac{dC_t}{dt} = \frac{bKC_t}{1 + KC_t} \quad (4)$$

Given the low pollutant concentrations typically employed in photocatalytic degradation studies, the term $KC_t \ll 1$, allowing the above expression to be simplified to the pseudo-first-order form (Equation (5)):

$$C_t = C_0 e^{-kt} \quad (5)$$

where b ($mg \cdot min^{-1} \cdot L^{-1}$), K ($L \cdot mg^{-1}$), and k (=b × K, min^{-1}) represent the reaction rate constant, the Langmuir adsorption equilibrium constant, and the apparent pseudo-first-order rate constant, respectively.

4. Photocatalytic Degradation Evaluation

The photocatalytic performance of the as-synthesized CaO, ZnO, Ag-doped ZnO, and Ag-doped CaO/ZnO nanocomposites was comparatively assessed using Rhodamine B (RhB) as a model organic pollutant. The conventional Langmuir–Hinshelwood pseudo-first-order model is widely employed to describe heterogeneous photocatalytic degradation [50]. However, its applicability can be limited when the reaction involves rapid initial pollutant removal, heterogeneous surface interactions, non-uniform distribution of active sites, or multiple degradation stages [50,51]. Under such conditions, the Behnajady–Modirshahla–Ghanbary (BMG) model [52] often provides a more suitable description of highly dynamic oxidation processes and, in some cases, fits experimental degradation data more accurately than conventional first-order kinetics [53]. In the present study, both models were therefore applied: the Langmuir–Hinshelwood model was used to describe

RhB degradation under visible light, which proceeded over 35 min, while the BMG model was applied to RhB degradation under UV irradiation within only 9 min.

The Ag-doped CaO/ZnO nanocomposite exhibited a markedly rapid photocatalytic response under UV light, achieving efficient Rhodamine B (RhB) removal within 9 min. Given this fast reaction rate, the BMG kinetic model was considered more appropriate for accurately capturing the degradation behavior under these conditions. The model is expressed as Equation (6):

$$\frac{t}{1-(C_t/C_0)} = m + nt \quad (6)$$

where C_0 and C_t represent the RhB concentration before irradiation and at irradiation time t, respectively. By defining the fractional degradation as Equation (7):

$$X = 1 - \frac{C_t}{C_0} \quad (7)$$

Equation (6) can be rewritten in its linear form as Equation (8):

$$\frac{t}{X} = m + nt \quad (8)$$

where t is the irradiation time in minutes, X is the fractional RhB removal, m is the intercept parameter expressed in minutes, and n is the slope parameter and is dimensionless. The linear plot of t/X versus t allows the two BMG parameters to be obtained from the intercept and slope, respectively. The initial apparent degradation-rate parameter is calculated as Equation (9):

$$r_0 = \frac{1}{m} \quad (9)$$

where r_0 is expressed in min^{-1}. The theoretical limiting degradation fraction is determined from Equation (10):

$$X_{max} = \frac{1}{n} \quad (10)$$

The BMG model is particularly useful for interpreting rapid photocatalytic processes in which the degradation rate changes significantly during irradiation [54]. This behavior may result from fast initial adsorption, the progressive occupation or deactivation of surface-active sites, and changes in the availability of photogenerated reactive species. The suitability of the BMG model should be evaluated by comparing its coefficient of determination and statistical error with those obtained from the pseudo-first-order and other kinetic models [54,55].

4.1. Dark Adsorption Evaluation

To establish the extent of adsorption–desorption equilibrium and evaluate the dark-adsorption affinity of the synthesized photocatalysts toward Rhodamine B (RhB), control experiments were performed under dark conditions (Figure 8). The pristine ZnO and CaO samples exhibited relatively low dark-adsorption removal efficiencies of 0.95% and 0.84%, respectively. Although pure CaO exhibits limited dye adsorption, its incorporation may alter surface accessibility and interfacial properties, theoretically contributing to the improved overall photocatalytic performance. In comparison, the binary ZnO/Ag composite displayed a noticeably improved adsorption efficiency of 3.68%, while the ternary Ag-doped CaO/ZnO nanocomposite exhibited the highest dark-adsorption capacity, reaching 4.87%. This progressive enhancement can be attributed to the increased specific surface area and mesoporous volume of the ternary system, together with the synergistic interfacial coupling between the CaO matrix and the Ag-modified ZnO nanostructures, which collectively provide a greater density of active adsorption sites and stronger electrostatic interactions for RhB capture before light-induced degradation [56].

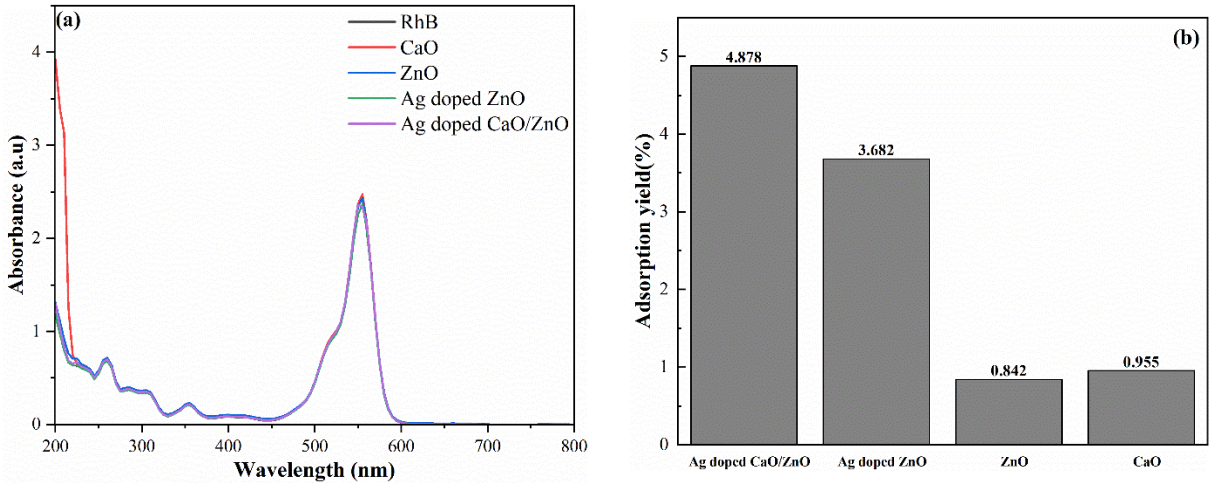

Figure 8. (**a**) UV-Vis absorption spectra and (**b**) dark adsorption yield (%) of Rhodamine B over pristine CaO, ZnO, Ag-doped ZnO, and Ag-doped CaO/ZnO nanocomposite samples. Experimental conditions: time = 40 min, $[RhB]_0$ = 10 mg/L, pH 5 and m = 0.08 g.

4.2. Comparative Photocatalytic Performance of ZnO, Ag-Doped ZnO, and Ag-Doped CaO/ZnO Heterostructure

The BMG kinetic plots exhibit a strong linear relationship between $t/[1 - (C_t/C_0)]$ and irradiation time, indicating that the model adequately describes the Rhodamine B (RhB) removal behavior of the investigated photocatalysts (Figure 9). The Ag-doped CaO/ZnO nanocomposite demonstrated a rapid photocatalytic response, achieving the selected RhB removal endpoint within 9 min.

The BMG parameters provide additional insight into the initial degradation behavior. Based on the plotted data, the approximate values of m were 0.392 min for ZnO, 0.134 min for Ag-doped ZnO, and 0.193 min for Ag-doped CaO/ZnO. These values correspond to initial apparent rate parameters of approximately 2.55, 7.45, and 5.19 min^{-1}, respectively (Table 2). Therefore, the BMG-derived initial-rate order was: Ag/ZnO > Ag/CaO/ZnO > ZnO. The higher initial apparent rate of the Ag-doped ZnO sample suggests that silver incorporation enhanced the early-stage degradation process, possibly through improved charge separation and more efficient interfacial electron transfer. The Ag-doped CaO/ZnO nanocomposite also exhibited favorable initial kinetics, while the eggshell-derived CaO component provided an additional basic and surface-reactive phase that may promote RhB adsorption and interfacial photocatalytic reactions. Thus, its rapid degradation response demonstrates the potential of valorizing eggshell waste as a functional CaO precursor for the development of efficient photocatalysts.

Table 2. Linear fitting parameters for photocatalytic degradation.

Catalyst	k (min^{-1})	R^2 (COD)	Adj. R^2
ZnO	2.55	0.996	0.996
Ag-doped ZnO	7.45	0.999	0.999
Ag-doped CaO/ZnO	5.19	0.999	0.999
CaO	-	~0.999	~0.999

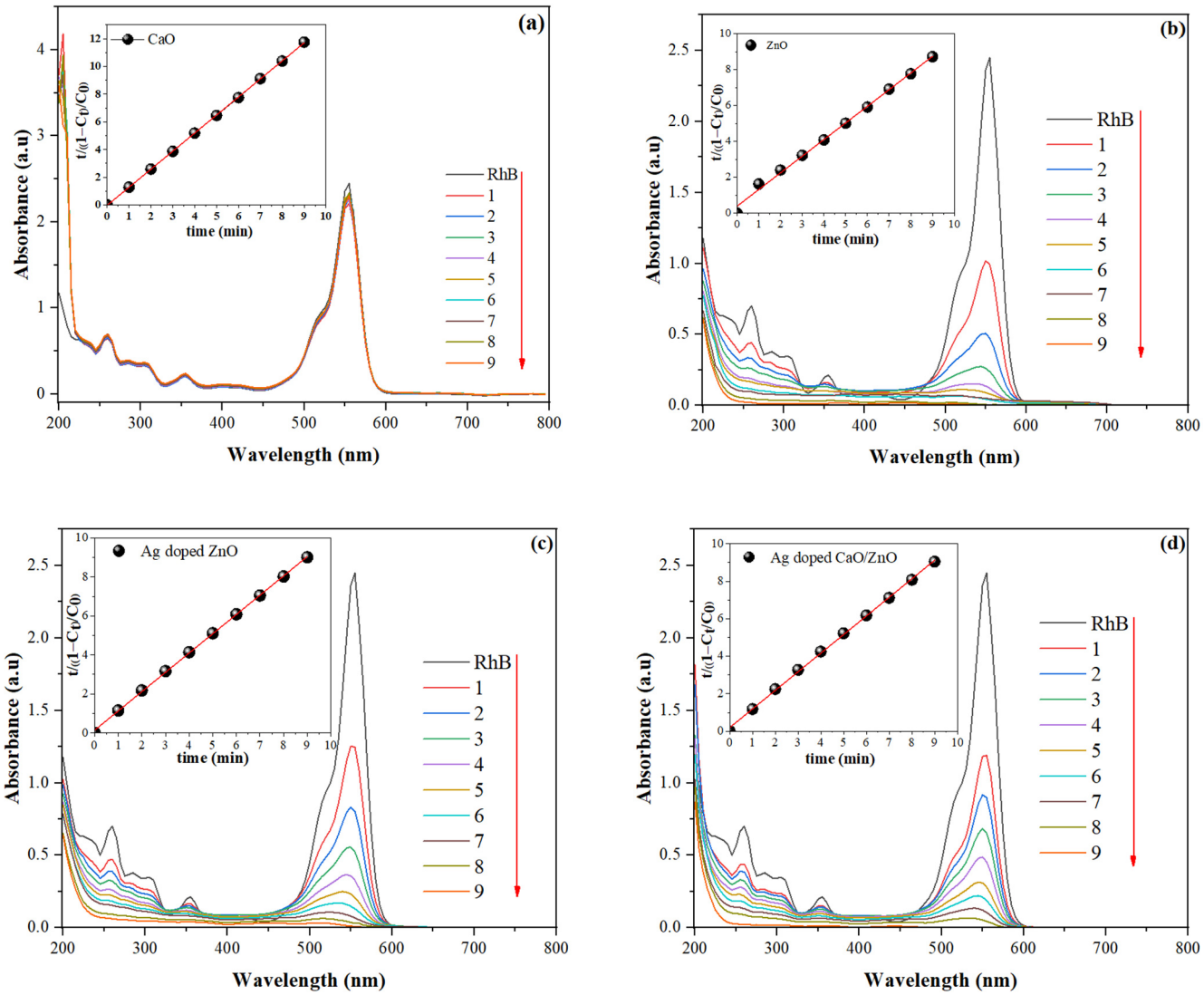

Figure 9. UV–Vis absorption spectra showing RhB degradation over (**a**) CaO, (**b**) ZnO, (**c**) Ag-doped ZnO, and (**d**) Ag-doped CaO/ZnO photocatalysts, along with the corresponding kinetic fits.

5. Chemical Oxygen Demand (COD) Removal and Extent of Mineralization

To assess mineralization beyond decolorization, the COD of the RhB solution was determined by the dichromate method before and after UV irradiation (Table 3). The COD (mg O_2/L) was calculated from the titration volumes as in Equation (11):

$$\mathrm{COD} = (8000 \times \mathrm{C} \times (\mathrm{V}_1 - \mathrm{V}_2))/\mathrm{V}_0 \quad (11)$$

where C is the concentration of the ferrous ammonium sulfate titrant (mol/L), V_1 and V_2 are the titrant volumes (mL) consumed by the blank and by the sample, respectively, and V_0 is the sample volume (mL). The COD removal efficiency was then calculated as in Equation (12):

$$\mathrm{COD\ removal}(\%) = (COD_0/COD_t)/COD_0 * 100 \quad (12)$$

where COD_0 and COD_t denote the chemical oxygen demand before irradiation and at irradiation time t, respectively.

Table 3. COD removal after RhB photodegradation over ZnO and Ag-doped CaO/ZnO.

Sample (UV Light)	COD (mg O_2/L)	COD Removal
Untreated RhB	464	–
RhB + ZnO	392	15.5%
RhB + Ag-doped CaO/ZnO	384	17.2%

To assess mineralization beyond decolorization, the COD of the RhB solution was determined by the dichromate method before and after UV irradiation (Table 3). The COD decreased from 464 mg O_2/L in the untreated solution to 392 mg O_2/L over ZnO and 384 mg O_2/L over the Ag-doped CaO/ZnO heterostructure, corresponding to removal efficiencies of 15.5% and 17.2%, respectively; the small difference (8 mg O_2/L) lies within the uncertainty of the titrimetric method. The modest COD removal, in sharp contrast with the complete decolorization achieved within 9 min, indicates that the process mainly cleaves the chromophore and N-deethylates the dye rather than fully mineralizing it, leaving colorless organic intermediates in solution, a decolorization-mineralization gap well documented for RhB photocatalysis [57].

6. Impact of Operational Parameter Optimization on RhB Photocatalytic Degradation Performance Under UV Light and Sunlight

a. Effect of Photocatalyst Dosage

To identify the optimal operating conditions and avoid unnecessary catalyst consumption, the effect of catalyst loading on the photocatalytic degradation of RhB was systematically examined. Experiments were performed at a fixed initial dye concentration (C0 = 10 mg/L) and solution pH of 5.0, with the Ag-doped CaO/ZnO nanocomposite dosage varied from 0.04 to 0.1 g (Figure 10a,b). As shown in Figure 10, the degradation efficiency increased progressively with increasing catalyst dosage, reaching a maximum at 0.08 g. This enhancement can be attributed to the corresponding increase in available active surface sites and adsorption centers, which promotes greater RhB uptake and facilitates the generation of reactive oxygen species (notably hydroxyl radicals, •OH) upon light irradiation [58]. However, a further increase in catalyst dosage beyond 0.08 g resulted in a marked decline in degradation efficiency, attributable to two interrelated effects: (i) excessive accumulation of suspended nanocomposite particles increase the turbidity of the reaction medium, thereby limiting light penetration [59]; and (ii) particle overcrowding intensifies light scattering and photon loss at saturated absorption levels, reducing the effective photon flux available for photoexcitation [60]. Accordingly, 0.08 g was selected as the optimal photocatalyst dosage for subsequent experiments.

b. Effect of Initial Dye Concentration

The effect of initial pollutant concentration on the photocatalytic performance of the Ag-doped CaO/ZnO nanocomposite was examined over the range of 3–12 mg/L (Figure 10c,d). As illustrated in Figure 10c, the degradation efficiency declined markedly from 100% to 91.33% with an increase in the initial dye concentration from 3 to 12 mg/L. This concentration-dependent behavior can be attributed to the limited availability of photogenerated reactive oxygen species relative to the increasing pollutant load [61]. At lower dye concentrations, a comparatively higher ratio of hydroxyl radicals (•OH) and superoxide radicals ($\bullet O_2^-$) to dye molecules is available, enabling rapid and sustained degradation [62]. As the dye concentration increases, however, a greater fraction of incident photons is absorbed directly by the dye molecules rather than reaching the catalyst surface, giving rise to an internal optical shielding (or screening) effect that reduces photon penetration depth

and suppresses electron–hole pair generation [59]. In parallel, the progressive saturation of active surface sites at higher dye loadings promotes competitive adsorption, thereby limiting the interaction of dissolved oxygen and water molecules with the catalyst surface and consequently reducing the rate of ROS generation [63].

c. Effect of Solution pH

The photocatalytic degradation of Rhodamine B (RhB) over the Ag-doped CaO/ZnO nanocomposite exhibited a pronounced pH dependence, reflecting the electrostatic interplay between the catalyst surface and the dye species [64]. This behavior is governed by two pH-sensitive parameters: (i) the surface charge of the catalyst, characterized by a point of zero charge (pHzpc) of 10.66, as determined by zeta-potential analysis (Figure 6), below which the surface is predominantly positively charged and above which it becomes neutral to negative; and (ii) the protonation state of RhB, dictated by its pKa (3.22), whereby the dye exists as a cationic species (RhB+, protonated diethylamino group) at pH < 3.22 and as a zwitterion (RhB±, coexisting carboxylate and protonated amine groups) at higher pH [64]. To assess this operational parameter, the degradation of RhB was monitored over an initial pH range of 3.0–11.0 (Figure 10e,f). A continuous decrease in dye concentration under irradiation was observed across the entire range, confirming the robustness of the photocatalytic process under both acidic and alkaline conditions. The highest degradation efficiencies were obtained at the natural (unadjusted) pH of 5 and at pH 11. At pH 5, favorable electrostatic attraction between the positively charged catalyst surface (pH < pHzpc) and the carboxylate group of zwitterionic RhB promotes efficient dye adsorption and subsequent radical-mediated oxidation [65]. At pH 11, the enhanced concentration of hydroxide ions favors the generation of hydroxyl radicals (•OH), compensating for the less favorable electrostatic configuration and sustaining high photo-oxidative activity [64,66]. Given its comparable efficiency and the absence of any need for pH adjustment (NaOH/HCl), the native pH 5 was selected as the optimal and most cost-effective operating condition for subsequent experiments.

d. Effect of coexisting inorganic ions on the degradation of RHB

Inorganic anions commonly present in natural and wastewater matrices can substantially modify the photocatalytic degradation of organic contaminants by interacting with the catalyst surface, photogenerated charge carriers, and reactive oxygen species (ROS). Their effects are highly system-dependent and may result in either enhanced or inhibited pollutant removal. Chloride, nitrate, sulfate, bicarbonate, carbonate, and phosphate species can compete for surface-active sites or consume reactive species such as hydroxyl radicals and photogenerated holes. Conversely, under specific irradiation and catalyst conditions, some anions may participate in the formation of secondary reactive species and thereby contribute to pollutant transformation. Consequently, the net influence of an anion depends on its chemical identity, concentration, solution pH, adsorption affinity, and the dominant reactive species generated by the photocatalytic system [67].

In the present study, the influence of the major inorganic anions was evaluated during the photocatalytic degradation of Rhodamine B (RhB) using the Ag-doped CaO/ZnO nanocomposite under UV light irradiation (Figure 10g,h). The salts investigated were sodium chloride (NaCl), sodium sulfate (Na_2SO_4), sodium carbonate (Na_2CO_3), sodium bicarbonate ($NaHCO_3$), potassium dihydrogen phosphate (KH_2PO_4), and potassium nitrate (KNO_3), corresponding to the anions Cl^-, SO_4^{2-}, CO_3^{2-}, HCO_3^-, $H_2PO_4^-$, and NO_3^-, respectively. Under the experimental conditions, nitrate, chloride, and sulfate ions did not produce any measurable inhibition in RhB removal, with degradation efficiencies of approximately 100% within 9 min. Carbonate and bicarbonate caused a moderate decrease in the photocatalytic efficiency, resulting in RhB removal yields of 96.96% and 82.63%,

respectively. The most pronounced inhibition was observed for dihydrogen phosphate, $H_2PO_4^-$, which reduced RhB removal from 100% to 60.49%.

The observed inhibitory effect can be attributed to competition between the anions and RhB molecules for reactive surface sites, together with the consumption or transformation of photogenerated reactive species. In particular, carbonate and bicarbonate may reduce the availability of hydroxyl radicals through radical-scavenging reactions, whereas phosphate species may interact more strongly with oxide surfaces and interfere with interfacial charge-transfer reactions. These effects are consistent with recent studies showing that bicarbonate, chloride, nitrate, and other dissolved ions can alter photocatalytic reaction rates by modifying the concentrations and contributions of hydroxyl and other reactive species. However, the direction and magnitude of the effect remain dependent on the photocatalyst, pollutant, ionic concentration, pH, and irradiation conditions [68,69].

Accordingly, the inhibitory influence of the tested anions on RhB photodegradation increased in the following order: $NO_3^- \approx Cl^- \approx SO_4^{2-} < CO_3^{2-} < HCO_3^- < H_2PO_4^-$.

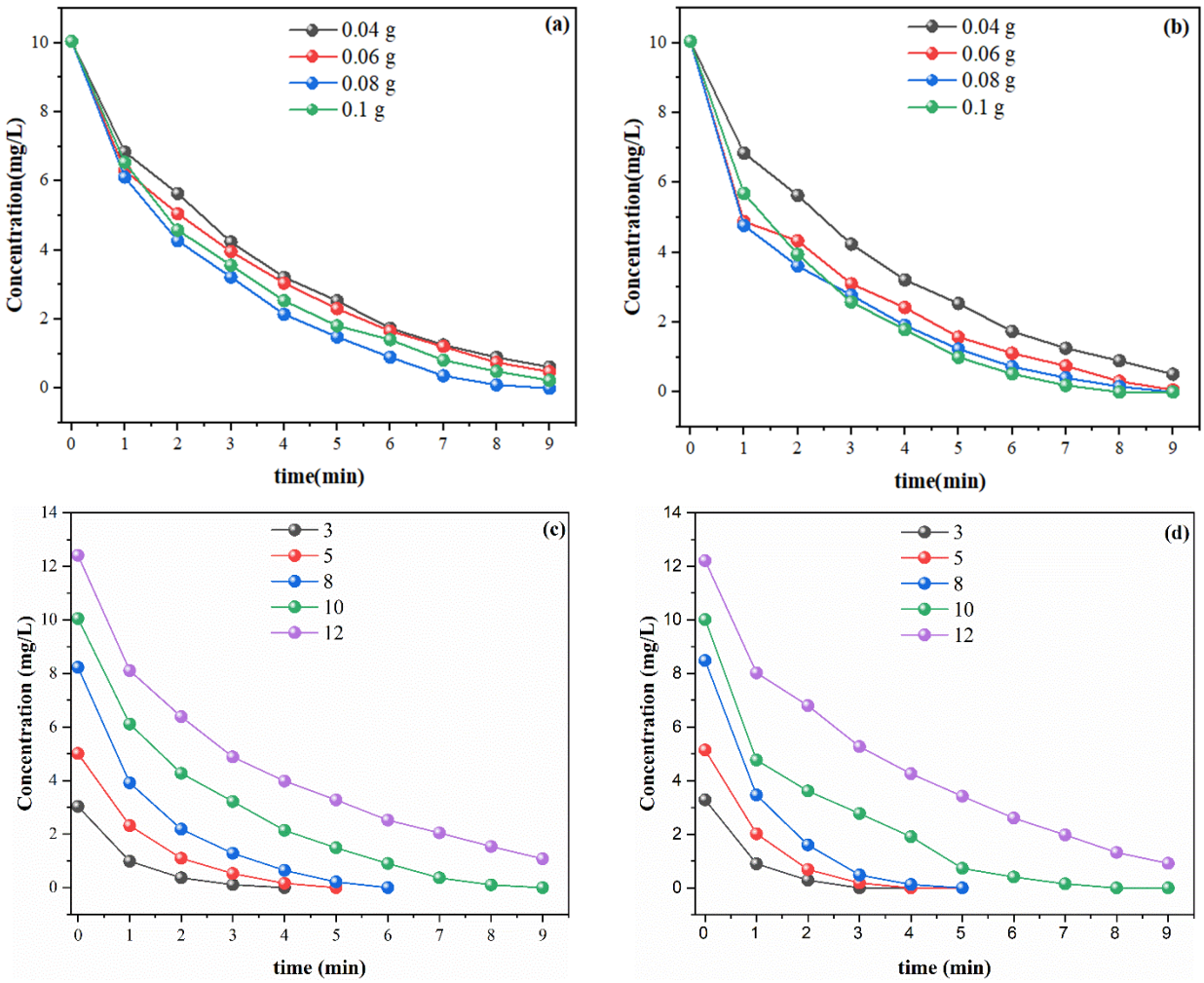

Figure 10. *Cont.*

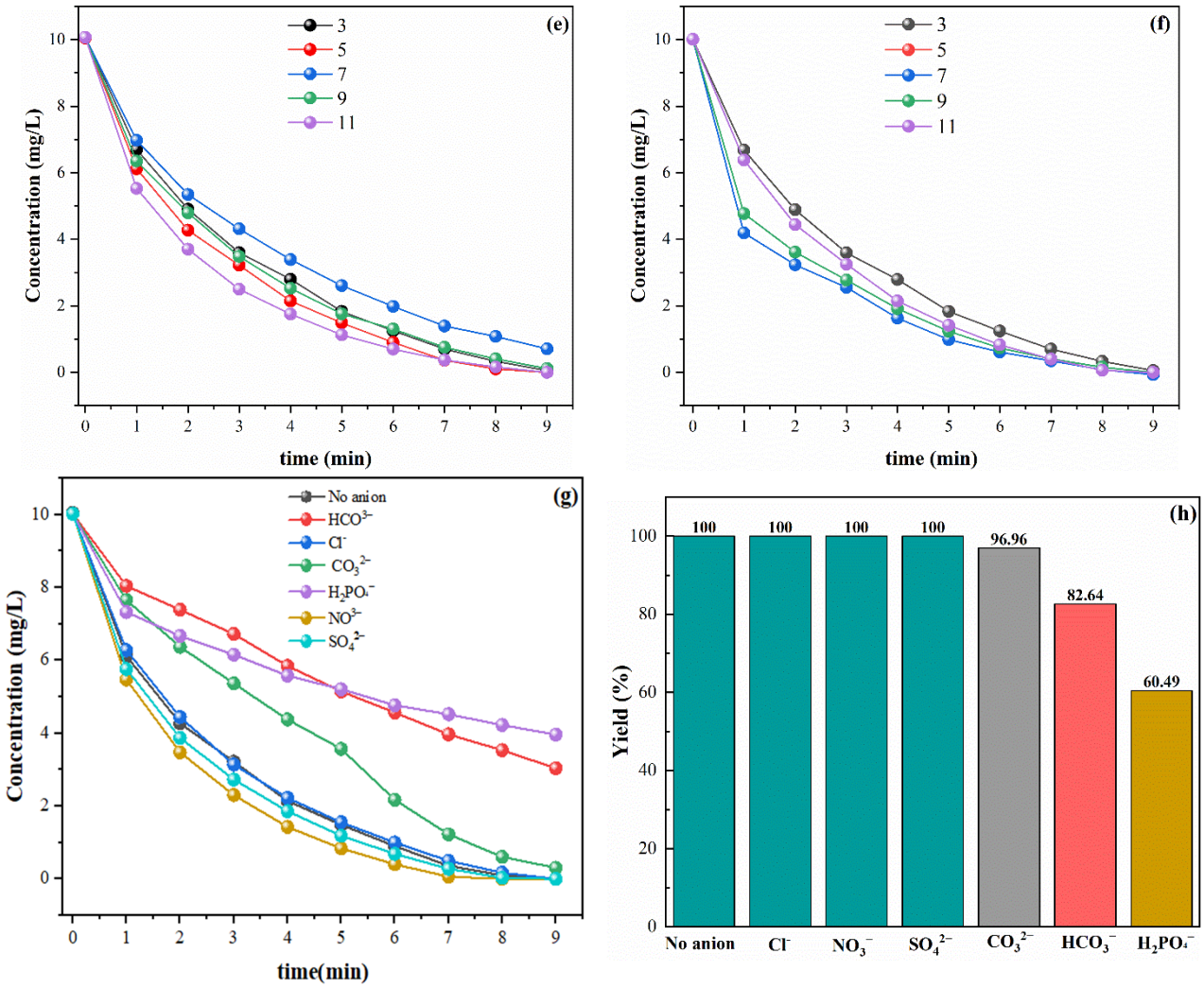

Figure 10. Effect of photocatalyst dosage (**a**,**b**), initial RhB concentration (**c**,**d**), and solution pH (**e**,**f**) on the photocatalytic degradation kinetics of RhB under UV light (**a**,**c**,**e**) and natural sunlight (**b**,**d**,**f**). Effect of coexisting inorganic anions on RhB degradation: (**g**) degradation kinetics and (**h**) corresponding degradation yield (%). Time = 9 min, $[RhB]_0$ = 10 mg/L, m = 0.08 g.

7. Mechanism of Ag-Doped CaO/ZnO Assisted Photocatalytic Degradation

The mechanism of photocatalysis by Ag-doped CaO/ZnO has already been described in depth in the literature [65,70]. When an aqueous Ag-doped CaO/ZnO dispersion is exposed to light energy above its bandgap energy (2.92 eV), conduction band electrons (e−CB) and valence band holes (h+VB) are photogenerated, triggering photocatalytic activity (Figure 11):

$$\text{Ag-doped CaO/ZnO} + h\nu \rightarrow e^-_{CB} + h^+_{VB} \quad (13)$$

The photogenerated holes combine with OH− or H_2O adsorbed on the catalyst surface, generating hydroxyl radicals (•OH) [71]:

$$h^+_{VB} + H_2O/OH^- \longrightarrow \cdot OH + H^+ \quad (14)$$

The superoxide radicals then react with H^+ to produce hydroperoxyl radicals (HO_2•):

$$O_2\cdot^- + H^+ \longrightarrow HO_2\cdot \quad (15)$$

Two hydroperoxyl radicals disproportionate to yield hydrogen peroxide, which is further reduced by CB electrons to generate additional hydroxyl radicals [70]:

$$2\,HO_2\cdot \longrightarrow H_2O_2 + O_2 \quad (16)$$

$$H_2O_2 + e^-{}_{CB} \longrightarrow HO\cdot + OH^- \quad (17)$$

Finally, the reactive oxidative species (•OH, $O_2\bullet^-$, $HO_2\bullet$) and photogenerated holes (h+VB) attack the adsorbed RhB molecules, leading to de-ethylation, chromophore cleavage, and mineralization into CO_2, H_2O, and inorganic ions [65,71]:

$$RhB + \{\cdot OH, O_2\cdot^-, HO_2\cdot, h^+{}_{VB}\} \longrightarrow Intermediates \longrightarrow CO_2 + H_2O + Inorganic\ ions \quad (18)$$

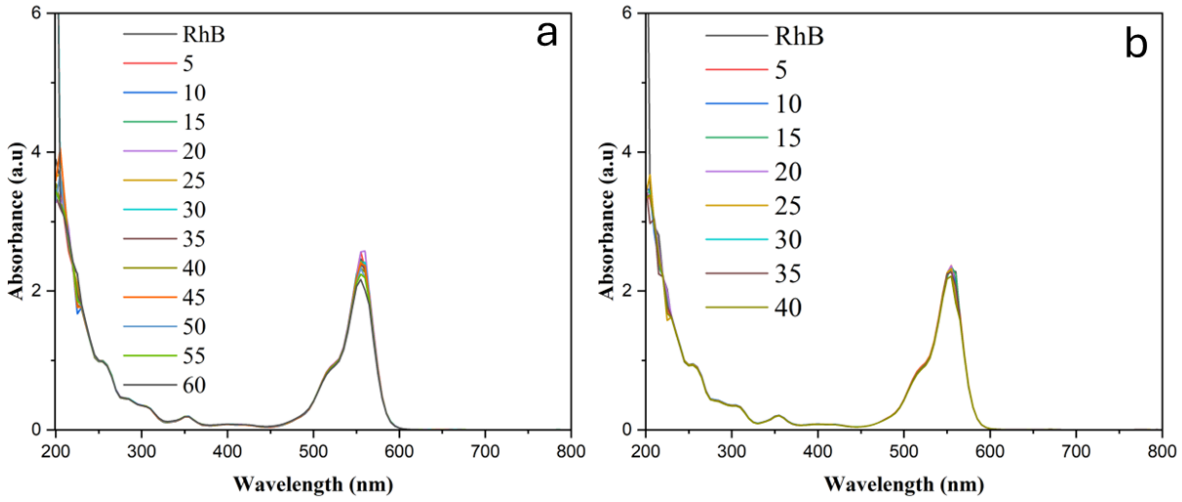

Figure 11. Control experiments showing: (**a**) RhB photostability under visible light in the absence of photocatalyst; and (**b**) dark adsorption–desorption equilibrium of RhB on the Ag-doped CaO/ZnO nanocomposite. Conditions: $[RhB]_0$ = 10 mg/L, pH 3, H_2O_2 = 10 µL.

8. H_2O_2-Assisted Photocatalytic Degradation of RhB over Ag-Doped CaO/ZnO Under Visible Light

a. Control Experiments Confirming RhB Photostability and Establishing Dark Adsorption–Desorption Equilibrium of the Ag-Doped CaO/ZnO/H_2O_2 System

To exclude passive contributions to dye removal, two control experiments were performed prior to the photocatalytic tests. First, to rule out direct photolysis or homogeneous H_2O_2 oxidation (Figure 12a), a blank experiment was conducted without any photocatalyst at pH 3, using 10 µL of H_2O_2 under 42 W visible-light irradiation. The characteristic RhB absorption band at λ_{max} = 554 nm remained essentially unchanged after 60 min, with degradation below 3%, confirming that neither visible light alone nor H_2O_2 in the absence of a catalyst is able to break down the RhB chromophore. This near-total stability reflects the fact that H_2O_2 cannot be photolyzed into hydroxyl radicals (HO•) under low-energy visible light ($\lambda > 400$ nm), a process that requires higher-energy UV photons ($\lambda < 300$ nm); moreover, although pH 3 is favorable for Fenton-type chemistry, the absence of a transition-metal ion or semiconductor surface precludes catalytic activation of H_2O_2 in this system. Second, the dark adsorption–desorption equilibrium (Figure 12b) was monitored for 40 min using 0.08 g of the Ag-doped CaO/ZnO nanocomposite in the presence of 10 µL H_2O_2 at pH 3, to establish the baseline contribution of passive mass transfer. Equilibrium in the principal RhB absorption band was reached within approximately 10 min, and the dark period was extended to 40 min to confirm complete surface saturation, with the UV–Vis spectra remaining fully superimposable beyond this point. The limited adsorption capacity

observed under these strongly acidic conditions is mainly attributed to electrostatic repulsion between the protonated, positively charged nanocomposite surface ($pH < pH_{pzc}$) and the cationic RhB species, while the invariant spectral profile between 10 and 40 min in the dark further confirms that H_2O_2 cannot be catalytically activated, nor generate reactive oxygen species, in the absence of light excitation. Collectively, these control experiments demonstrate that RhB is photochemically stable under visible light and that the dye removal observed under irradiation proceeds through a genuine light-driven photocatalytic pathway, mediated by photogenerated charge carriers and reactive oxygen species at the nanocomposite surface, rather than through direct photolysis, uncatalyzed H_2O_2 oxidation, or surface physisorption alone.

b. Synergistic effect of H_2O_2 addition under visible light irradiation

The photocatalytic activity of the synthesized material was systematically evaluated under both UV and visible light irradiation (Figure 12a,b). Under UV light, the photocatalyst exhibited ultra-fast performance, achieving complete degradation (100%) within 9 min. This outstanding activity is directly correlated with the material's optical bandgap of 2.92 eV, which enables efficient band-to-band excitation and abundant photogeneration of electron-hole (e^-/h^+) pairs under UV photons. Conversely, under visible light irradiation, the degradation efficiency dropped markedly to 25.48%, owing to the limited visible-light harvesting capability of the wide-bandgap semiconductor coupled with rapid charge-carrier recombination.

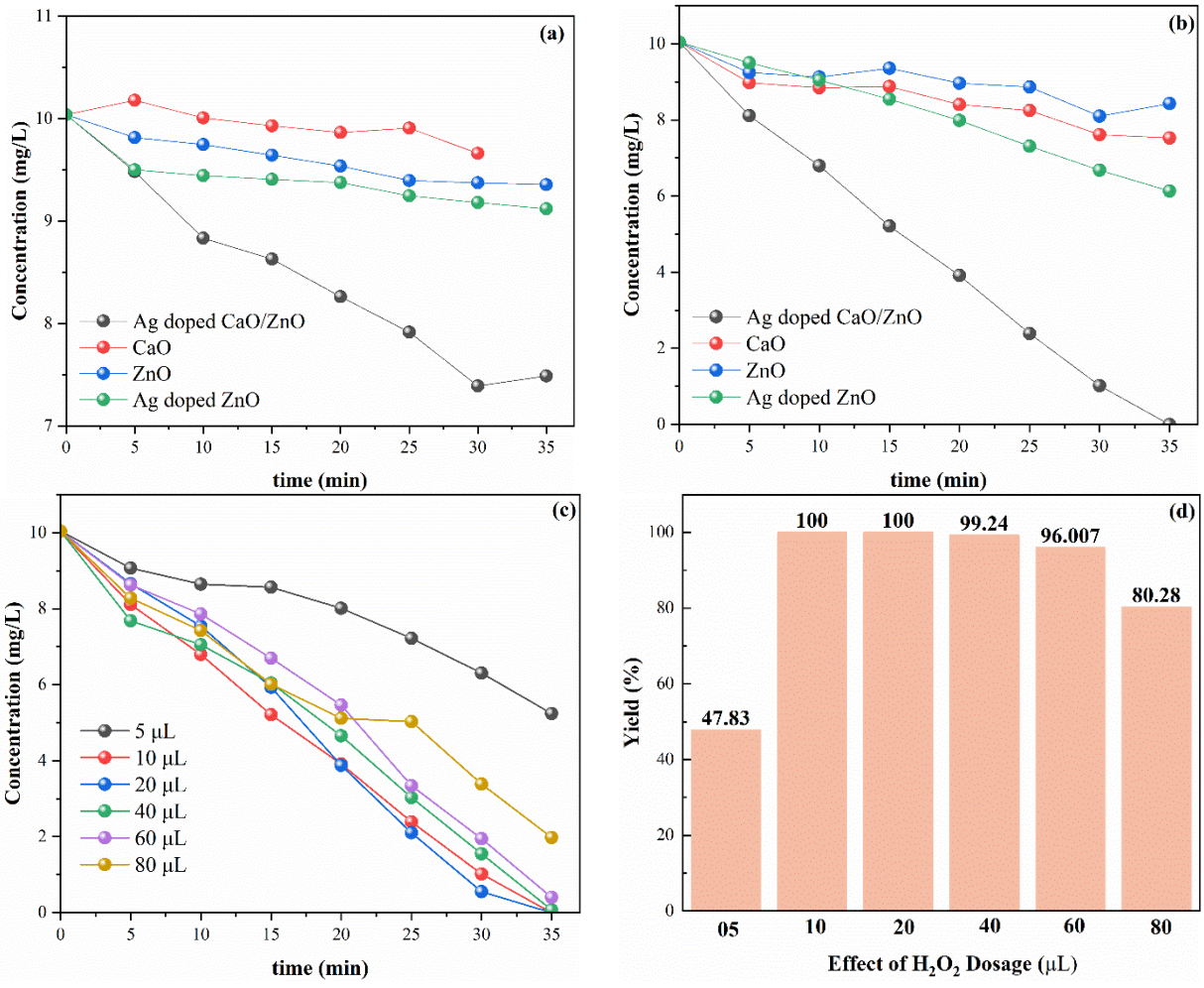

Figure 12. *Cont.*

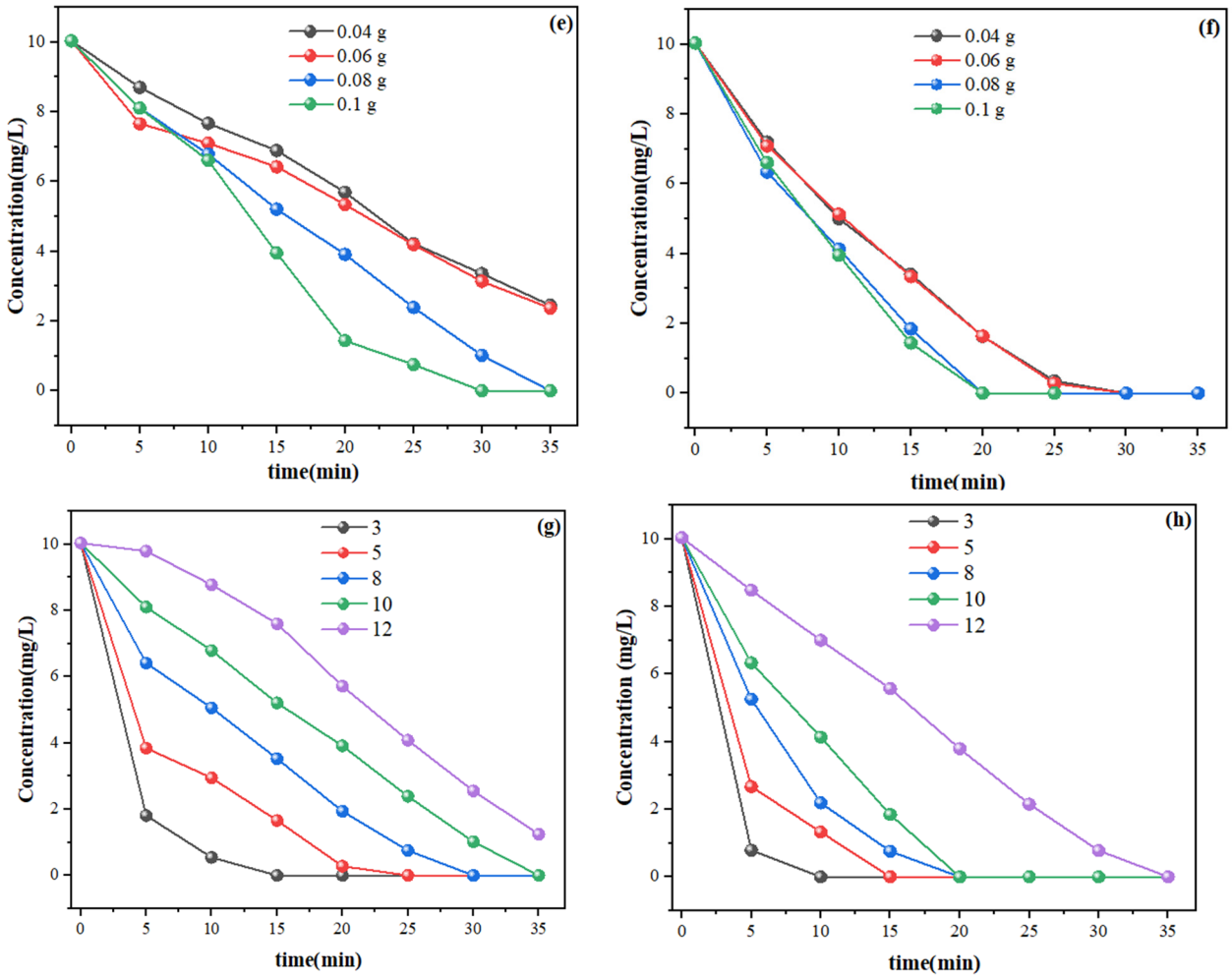

Figure 12. Photocatalytic degration of RhB over CaO, ZnO, Ag-doped ZnO, and Ag-doped CaO/ZnO under visible light: (**a**) in the absence of H_2O_2 and (**b**) in the presence of H_2O_2. Effect of H_2O_2 dosage on RhB degradation: (**c**) kinetic profiles and (**d**) corresponding degradation efficiency (%). Effect of catalyst dosage under artificial visible light (**e**) and solar light (**f**), and effect of initial RhB concentration under artificial visible light (**g**) and solar light (**h**). Experimental conditions: t = 35 min, $[RhB]_0$ = 10 mg/L, pH 3.

Interestingly, the addition of H_2O_2 to the photocatalytic system under visible light led to a remarkable enhancement, boosting the degradation efficiency to 100% within 35 min. This synergistic enhancement can be ascribed to dual mechanisms. First, H_2O_2 serves as an effective electron acceptor in the conduction band:

$$H_2O_2 + e^- \rightarrow {}^{\cdot}OH + OH^- \quad (19)$$

thereby suppressing e^-/h^+ recombination and preserving valence-band holes (h^+) for direct oxidation. Second, the decomposition of H_2O_2 yields an increased concentration of highly reactive hydroxyl radicals (·OH). Consequently, coupling the photocatalyst with H_2O_2 effectively overcomes the visible-light absorption constraint and significantly accelerates the degradation kinetics (Table 4).

Table 4. Kinetic parameters for RhB photocatalytic degradation under visible light.

Reaction Condition	k (min^{-1})	R^2 (COD)	Adj R^2
SC in absence of H_2O_2	0.00763	0.962	0.956
SC in presence of H_2O_2	0.02953	0.999	0.998

c. Optimization of H_2O_2 Dosage for Enhanced Photocatalytic Performance

The influence of hydrogen peroxide concentration on RhB degradation was evaluated under visible-light irradiation at pH 3 by varying the H_2O_2 dosage from 5 to 80 µL, and the resulting profile followed a characteristic volcano-shaped trend. Increasing the H_2O_2 dosage up to 10–20 µL markedly enhanced the removal efficiency, affording complete degradation within 35 min, with yields of 47.83% at 5 µL and 100% at both 10 and 20 µL (Figure 12c,d). This enhancement arises from the role of H_2O_2 as an electron acceptor for the photogenerated conduction band electrons ($e-_{CB}$), which suppresses electron–hole recombination and thereby promotes the generation of hydroxyl radicals (·OH) responsible for pollutant oxidation. Beyond this optimum, however, further addition of H_2O_2 (40, 60, and 80 µL) progressively diminished the photocatalytic activity, with yields declining to 99.2%, 96%, and 80%, respectively. This inhibition is attributed to the scavenging of ·OH radicals by excess H_2O_2, which consumes the primary oxidizing species and generates the considerably less reactive perhydroxyl radicals ($HO_2^{\cdot}$). Accordingly, 10 µL was established as the optimal H_2O_2 dosage for the present photocatalytic system.

d. Effect of Catalyst Dosage on RhB Photodegradation

The influence of Ag-doped CaO/ZnO loading (0.04–0.1 g) on the photocatalytic degradation of Rhodamine B (10 mg/L) at pH 3, in the presence of 10 µL H_2O_2, was evaluated under both 42 W artificial visible light and natural sunlight (117.7 klux) (Figure 12e,f). Under artificial visible-light irradiation, increasing the catalyst mass from 0.04 g to 0.1 g markedly accelerated the degradation kinetics. At 35 min under artificial visible light (42 W), removal efficiencies of 75.56% and 76.38% were recorded for loadings of 0.04 g and 0.06 g, respectively, whereas the higher loadings (0.08 g and 0.1 g) had already achieved complete (100%) dye elimination. Under natural sunlight, by contrast, complete degradation was reached within 30 min for 0.04 g and 0.06 g, and within 20 min for 0.08 g and 0.1 g. This dosage-dependent enhancement is ascribed to the greater availability of catalytically active surface sites and the improved light-harvesting capacity at higher loadings, which together favor more efficient (e^-/h^+) pair separation and accelerate the interfacial conversion of H_2O_2 into highly reactive (·OH) radicals. Under these conditions, 0.08 g was identified as the optimal catalyst loading, balancing maximum activity with reagent economy. Under natural sunlight, degradation proceeded even more efficiently than under artificial illumination: complete decolorization was attained within 20 min for the higher loadings (0.08 g and 0.1 g), whereas the lower loadings (0.04 g and 0.06 g) required 30 min to reach 100% degradation. This superior solar performance is primarily attributed to the localized surface plasmon resonance (LSPR) of the silver nanoparticles, combined with the higher photon flux characteristic of natural sunlight. Taken together, these results confirm the strong potential of Ag-doped CaO/ZnO as an efficient, solar-activated photocatalyst for practical and sustainable wastewater treatment applications (Table 5).

Table 5. Comparison of Ag-doped ZnO/CaO-type photocatalysts for dye and pharmaceutical pollutant degradation.

Catalyst	Target Pollutant	Synthesis Method	Light Source	Degradation Time	Efficiency	Reference
Ag-doped CaO/ZnO	Rhodamine B (dye)	Eggshell-derived CaO + co-precipitation, calcined 400 °C/2 h	UV-A/Visible	9 min/35 min	100% (both)	**This study**

Table 5. *Cont.*

Catalyst	Target Pollutant	Synthesis Method	Light Source	Degradation Time	Efficiency	Reference
Ag-doped ZnO/CaO (Caccinia macranthera extract)	Methylene blue (dye)	Green (bio-mediated) synthesis, calcined 700 °C/2 h	—	100 min	90%	[72]
CaO (eggshell-derived) tribo/solar-tribocatalyst	Rhodamine B (dye)	Calcination, 900 °C	Ambient light/ sunlight (tribo-assisted)	240 min	33% (photo only), 91% (solar-tribo)	[73]
ZnO/Ag nanowire composite film	Rhodamine B (dye)	Sol–gel	UV (365 nm)	40 min	90%	[65]
Au/Ag-decorated ZnO	Tetracycline + Methylene blue (co-degradation)	Chemical reduction (hydrazine hydrate)	Visible	120 min	95% (TC)/80% (MB)	[74]
Ag-doped ZnO/CuO	Tetracycline + organic dyes	Green synthesis (Sclerorhachis leptoclada extract)	Visible	—	Efficient degradation reported	[75]
Ag-doped kaolinite/ZnO quantum dots	Rhodamine B (dye)	Pyrofabrication from zinc nitrate, silver nitrate, and kaolinite	Solar irradiation	150 min	96.93%	[76]

e. Effect of Initial Dye Concentration

The effect of initial RhB concentration (3–12 mg/L) on the photocatalytic degradation efficiency of the Ag-doped CaO/ZnO/H_2O_2 system at pH 3 was investigated under both artificial visible light and natural sunlight (Figure 12g,h). For both irradiation sources, the degradation rate decreased progressively as the initial dye concentration increased. Under artificial visible light, the time required for complete removal increased from 15 min at 3 mg/L to 35 min at 10 mg/L, whereas under natural sunlight it increased from 10 min to 20 min over the same concentration range. At the highest concentration (12 mg/L), the difference between the two sources became more pronounced: only ~88% of RhB was removed after 35 min under visible light, compared with complete removal under sunlight. This trend can be attributed to two combined effects. First, at higher dye concentrations, a greater number of RhB molecules are adsorbed on the catalyst surface, progressively saturating the available active sites and thereby limiting further interaction with photogenerated reactive species (•OH, h^+). Second, the increased optical density of the solution at higher concentrations reduces photon penetration and light absorption by the catalyst, decreasing the overall photon flux reaching its surface and, consequently, the generation rate of electron-hole pairs. Comparing the two light sources, degradation under natural sunlight (Figure 12h) was consistently faster than under artificial visible light (Figure 12g) at equivalent concentrations. This is likely due to the broader spectral range and higher photon flux of natural sunlight, which enhance the photoactivation of the Ag-doped CaO/ZnO nanocomposite and promote more efficient activation of H_2O_2 into hydroxyl radicals.

9. Scavenger-Based Identification of Reactive Species and Charge Carriers

To elucidate the reactive oxygen species (ROS) responsible for RhB degradation over the Ag-doped CaO/ZnO nanocomposite, selective scavenger experiments (Figure 13a,b)

were conducted under both visible-light (42 W, pH 3, H_2O_2-assisted) and UV irradiation. Isopropanol (IPA), ethylenediaminetetraacetic acid (EDTA), silver nitrate ($AgNO_3$), and benzoquinone (BQ) were employed to selectively scavenge hydroxyl radicals (·OH), photogenerated holes (h^+), photogenerated electrons (e^-), and superoxide radicals ($\cdot O_2^-$), respectively. In the absence of any scavenger, complete decolorization (100%) was achieved under both irradiation modes, confirming the intrinsic photocatalytic efficiency of the nanocomposite. Nevertheless, the two excitation sources gave rise to distinctly different dominant degradation pathways. Under visible light, the degradation efficiency was most strongly suppressed by BQ (33.45%), followed by IPA (53.09%) and EDTA (70.25%), whereas $AgNO_3$ exerted only a marginal effect (99.37%). This trend establishes the reactivity order $\cdot O_2^- >$ ·OH > $h^+ \gg e^-$, identifying superoxide radicals as the predominant reactive species, with hydroxyl radicals and photogenerated holes contributing to a secondary yet notable extent. Under UV irradiation, by contrast, IPA produced the most pronounced inhibition (18.25%), closely followed by EDTA (19.98%), while BQ (53.08%) and $AgNO_3$ (60.08%) induced comparatively moderate reductions, pointing to a reactivity order dominated by ·OH and h^+, with superoxide radicals and electrons playing a subordinate role.

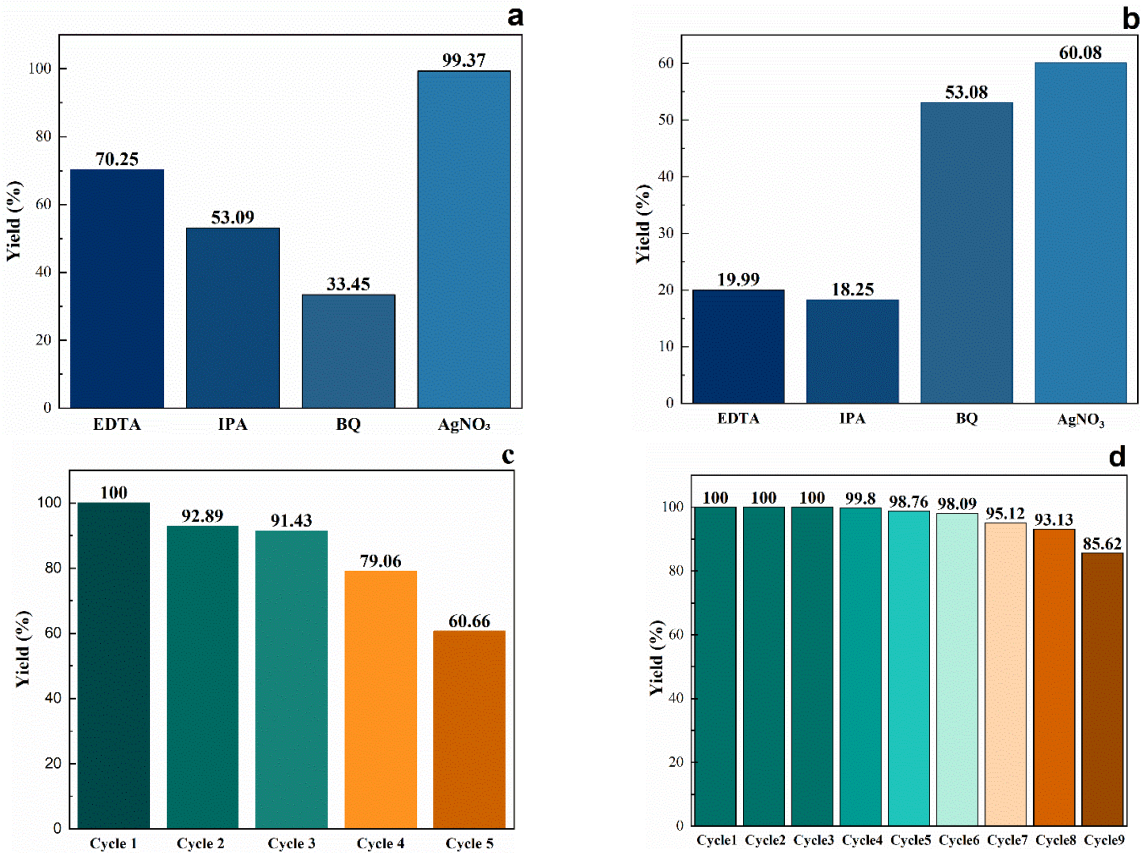

Figure 13. Effect of Selective Scavengers (**a**,**b**) and Recyclability (**c**,**d**) on the Photocatalytic Degradation of Rhodamine B by Ag-doped CaO/ZnO under Visible Light (**a**,**c**) and UV Light (**b**,**d**).

10. Reusability and Regeneration Performance of the Ag-Doped CaO/ZnO Photocatalyst

The reusability and regeneration performance of the Ag-doped CaO/ZnO photocatalyst was evaluated over multiple successive degradation cycles under two different conditions to assess its structural and catalytic stability (Figure 13).

(c)-In the presence of H_2O_2 under visible light: the photocatalyst maintained high activity (>91%) over the first three cycles but underwent pronounced deactivation thereafter,

retaining only 60.66% of its initial efficiency by the fifth cycle. This progressive decrease (~40% loss after 5 cycles) can be attributed to several factors, including the oxidative etching effect of H_2O_2 on the catalyst surface, partial leaching of active sites, blockage of active sites by adsorbed degradation intermediates, and slight catalyst mass loss during repeated recovery/washing steps.

(d)-In the absence of H_2O_2 under UV light: The photocatalyst exhibited markedly superior stability, retaining 100% yield through the first three cycles and only slightly declining to 99.8%, 98.76%, 98.09%, 95.12%, 93.13%, and 85.62% by the ninth cycle. This confirms excellent structural robustness and reusability of the Ag-doped CaO/ZnO nanocomposite when relying solely on UV-induced electron–hole pair generation, without the additional oxidative stress introduced by H_2O_2.

11. Conclusions

This study demonstrated a sustainable waste-to-value strategy for producing an Ag-doped CaO/ZnO photocatalyst from chicken eggshell waste, integrating 60 wt% CaO, 35 wt% ZnO, and 5 wt% Ag. Eggshells were converted to crystalline CaO at 900 °C, with 30 min of calcination sufficient to achieve the target phase while minimizing energy consumption. The optimized CaO was combined with ZnO and Ag via green co-precipitation and thermal treatment, yielding a multicomponent material in which Ca, Zn, O, and Ag were detected by EDX, Ca-O and Zn-O vibrational bands were identified by FTIR, and crystalline CaO and ZnO phases were confirmed by XRD. Structural and textural analyses confirmed retention of the ZnO crystalline framework, a mesoporous architecture (14.88 m^2/g, 0.088 cm^3/g, 23.70 nm), and a reduced bandgap from 3.15 eV (pristine ZnO) to 2.92 eV (ternary composite), indicating enhanced light absorption and interfacial charge transfer. The nanocomposite outperformed individual CaO and ZnO, achieving RhB removal in 9 min under UV, 25.48% under visible light alone, and 100% in 35 min with H_2O_2, confirming the synergistic role of H_2O_2 as an electron acceptor and •OH precursor. Under natural sunlight with H_2O_2, degradation occurred within 20 min at higher loadings. Scavenger tests may reveal condition-dependent mechanisms: •OH and h^+ dominated under UV, while $•O_2^-$ and •OH prevailed under visible light/H_2O_2, with h^+ contributing secondarily. Stability differed markedly: the UV system retained 85.62% activity after nine cycles, whereas the visible-light/H_2O_2 system dropped to 60.66% after five cycles, suggesting H_2O_2 accelerates deactivation through surface oxidation, active-site modification, or catalyst loss. Overall, the Ag-doped CaO/ZnO nanocomposite combines the surface reactivity of eggshell-derived CaO, the semiconducting activity of ZnO, and the charge-transfer and light-harvesting benefits of Ag, demonstrating strong potential as a low-cost, sustainable photocatalyst for dye-contaminated water. Future work should include LC-MS identification of degradation intermediates, TOC analysis, post-cycle XPS and TEM analyses, and real textile wastewater experiments to confirm long-term stability and environmental safety before scale-up.

Author Contributions: Conceptualization, S.K., Y.S. and L.M.; methodology, S.K., Y.S. and L.M.; investigation, S.K., Y.S. and L.M.; data curation, S.K., Y.S. and L.M.; formal analysis, S.K., Y.S. and L.M.; writing—original draft preparation, S.K., L.M. and G.V.; writing—review and editing, S.K., L.M. and G.V.; visualization, S.K., L.M., H.B. and G.V.; supervision, H.B., T.H.T. and L.M.; project administration, T.H.T., F.M.A. and H.B. All authors have read and agreed to the published version of the manuscript.

Funding: This research work was funded by Umm Al-Qura University, Saudi Arabia under grant number 26UQU4310078GSSR02.

Data Availability Statement: Data supporting the findings of this study are available within the article. Further inquiries can be directed to the corresponding authors.

Acknowledgments: The authors extend their appreciation to Umm Al-Qura University, Saudi Arabia for funding this research work through grant number 26UQU4310078GSSR02.

Conflicts of Interest: The authors declare no conflict of interest.

References

1. Sravan, J.S.; Matsakas, L.; Sarkar, O. Advances in Biological Wastewater Treatment Processes: Focus on Low-Carbon Energy and Resource Recovery in Biorefinery Context. *Bioengineering* **2024**, *11*, 281. [CrossRef] [PubMed]
2. Patel, R.; Mahabari, K.; Patel, K.; Patel, M.; Jadhav, A.H.; Dharaskar, S.; Karri, R.R.; Chaudhari, N. MoS2/MXene Composite Material for High-Performance Removal of Rhodamine B Dye: Synthesis and Application. *Sci. Rep.* **2025**, *15*, 42099. [CrossRef] [PubMed]
3. Zahi, S.E.; Hidalgo, M.C.; Navío, J.A.; Heddam, S.; Yacine, K. Photo-Assisted Degradation of Rhodamine B with H_2O_2: Kinetics, Modern Machine Learning Prediction, and Insights into a Novel Iron Oxide Catalyst. *J. Photochem. Photobiol. A Chem.* **2026**, *472*, 116739. [CrossRef]
4. Bollinger, J.-C.; Lima, E.C.; Mouni, L.; Salvestrini, S.; Tran, H.N. Molecular Properties of Methylene Blue, a Common Probe in Sorption and Degradation Studies: A Review. *Environ. Chem. Lett.* **2025**, *23*, 1403–1424. [CrossRef]
5. Zhang, M.; Du, J.; Zheng, X.; Ma, A. The Preparation of ZnFe2O4 from Coal Gangue for Use as a Photocatalytic Reagent in the Purification of Dye Wastewater via the PMS Reaction. *Materials* **2026**, *19*, 169. [CrossRef] [PubMed]
6. Yang, Y.; Zhang, Y.; Yang, F.; Wang, X.; Guo, Y.; Sun, L.; Li, S. From Tetracycline to Sulfamethoxazole: Photocatalytic Degradation and Mechanistic Insights in Aquatic Environments. *Rare Met.* **2026**, *45*, e70625. [CrossRef]
7. Liang, F.; Liu, Y.; Wang, X.; Yu, X.; Yang, F.; Guo, Y.; Ma, D.; Li, S. Engineering Organic-Inorganic Tetra (4-Carboxyphenyl) Porphyrin/Bi4O5Br2 S-Scheme Interfaces for Efficient Photoinduced Carrier Separation and Antibiotic Degradation. *Acta Phys.-Chim. Sin.* **2026**, *42*, 100383. [CrossRef]
8. Zhang, J.; Yu, G.; Yang, C.; Zhao, W.; Duan, Z.; Liu, H.; Li, S. Reinforced ROS Generation and Anti-Photocorrosion for Boosted Photooxidation Disinfection by IEF-Enhanced Type II Charge Carrier Dynamics. *SusMat* **2025**, *5*. [CrossRef]
9. Beena, V.; Parvathiraja, C.; Paulkumar, K.; Gupta, J.K.; Almutairi, T.M.; Mouni, L. Bio-Engineered NiO Nanoparticles for Photocatalytic and Antibacterial Treatments. *J. Dispers. Sci. Technol.* **2026**, *47*, 1938–1950. [CrossRef]
10. Halim, O.M.A.; Mustapha, N.H.; Mohd Fudzi, S.N.; Azhar, R.; Zanal, N.I.N.; Nazua, N.F.; Nordin, A.H.; Mohd Azami, M.S.; Mohd Ishak, M.A.; Ismail, W.I.N.W.; et al. A Review on Modified ZnO for the Effective Degradation of Methylene Blue and Rhodamine B. *Results Surf. Interfaces* **2025**, *18*, 100408. [CrossRef]
11. Tebbi, S.O.; Amrane, A.; Boudraa, R.; Bollinger, J.-C.; Salvestrini, S.; Kanjal, M.I.; Tiri, A.; Belkhiri, L.; Alharthi, M.N.; Mouni, L. Green synthesis of sustainable and cost-effective TiO_2–SiO_2–Fe_2O_3 heterojunction nanocomposites for Rhodamine B dye degradation under sunlight. *Water* **2025**, *17*, 168. [CrossRef]
12. Boudraa, R.; Talantikite-Touati, D.; Djermoune, A.; Souici, A.; Kebir, M.; Merzeg, F.A.; Amrane, A.; Bollinger, J.-C.; Mouni, L. Comprehensive Characterization and Unprecedented Photocatalytic Efficacy of TiO_2 -CuO-La_2O_3 and TiO_2 -CuO-Bi_2O_3 Nanocomposites: A Novel Approach to Environmental Remediation. *Mater. Sci. Eng. B* **2025**, *312*, 117863.
13. Hossain, E.; Lee, J.S.; Kwon, K.S. Photocatalytic Degradation of Hydrothermally Grown Zinc Oxide Nanorods on a Silver Seed Layer. *ACS Omega* **2025**, *10*, 5708–5721. [CrossRef] [PubMed] [PubMed Central]
14. Liang, Y.-C.; Yang, H.-C.; Jung, H. Surface Modification of Porous ZnO Sheets with Ag and Ag2O Nanoparticles for Enhanced Photoelectrochemical and Photocatalytic Performance. *J. Sci. Adv. Mater. Devices* **2025**, *10*, 101020. [CrossRef]
15. Celshia, S.S.; Muthamizh, S.; Varman, K.A.; Balu, S. Synthesis and Visible Light-Driven Photocatalytic Performance of Plasmonic Ag@ZnO Nanocomposites for Rhodamine B Degradation. *J. Mater. Sci. Mater. Electron.* **2026**, *37*, 1750. [CrossRef]
16. Yakub, T.; Asthana, A.; Sanwaria, S.; Singh, A.K.; Carabineiro, S.A.C. Highly Efficient Graphene Oxide/Zinc Oxide/Lignin Catalyst for Photocatalytic Degradation of Methylene Blue and Gentian Violet. *Nanomaterials* **2025**, *15*, 1342. [CrossRef] [PubMed]
17. Benazouz, K.; Bouchelkia, N.; Imessaoudene, A.; Bollinger, J.-C.; Amrane, A.; Hicham, Z.; Mouni, L. Efficient and Low-Cost Water Remediation for Chitosan Derived from Shrimp Waste, an Ecofriendly Material: Kinetics Modeling, Response Surface Methodology Optimization, and Mechanism. *Water* **2023**, *15*, 3728. [CrossRef]
18. Bouchelkia, N.; Tahraoui, H.; Benazouz, K.; Mameri, A.; Boudraa, R.; Moussa, H.; Hamri, N.; Merdoud, R.; Belkacemi, H.; Zoukel, A.; et al. Optimizing Adsorption Efficiency: A Novel Application of SVM_Boosting_IGWO for Methylene Blue Dye Removal Using Low-Cost Fruit Peels Adsorbents. *Chemom. Intell. Lab. Syst.* **2025**, *261*, 105377. [CrossRef]
19. Adaikalam, K.; Hussain, S.; Anbu, P.; Rajaram, A.; Sivanesan, I.; Kim, H.-S. Eco-Friendly Facile Conversion of Waste Eggshells into CaO Nanoparticles for Environmental Applications. *Nanomaterials* **2024**, *14*, 1620. [CrossRef] [PubMed]

20. Dabas, S. Metal and Metal Oxide Based Nanoremediation: A Sustainable Alternative. *Discov. Mater.* **2025**, *5*, 67. [CrossRef]
21. Sharma, P.; Ganguly, M.; Doi, A. Application of the Synergism between Eggshells and Copper in Nanotechnology. *Nanoscale Adv.* **2025**, *7*, 3914–3940. [CrossRef] [PubMed]
22. Gebretsadik, A.; Kefale, B.; Sori, C.; Tsegaye, D.; Ananda Murthy, H.C.; Abebe, B. Cu-Doped ZnO/Ag/CuO Heterostructure: Superior Photocatalysis and Charge Transfer. *RSC Adv.* **2024**, *14*, 29763–29773. [CrossRef] [PubMed]
23. Almássy, B.; Balázsi, K.; Balázsi, C. Preparation and Characterization of Hydroxyapatite from Eggshells via a Basic Route Using Attritor Milling. *Nanomaterials* **2026**, *16*, 899. [CrossRef] [PubMed]
24. Schiopu, A.-G.; Oproescu, M.; Berevoianu, A.; Mărginean, R.; Ionașcu, L.; Năstasă, V.; Dinache, A.; Mereuță, P.; KeunHwan, K.; Istrate, D.; et al. Biogenic Synthesis of Calcium-Based Powders from Marine Mollusk Shells: Comparative Characterization and Antibacterial Potential. *Materials* **2025**, *18*, 3331. [CrossRef] [PubMed]
25. Kalaycı, T.; Altuğ, D.T.; Kınaytürk, N.K.; Tunalı, B. Characterization and Potential Usage of Selected Eggshell Species. *Sci. Rep.* **2025**, *15*, 6241. [CrossRef] [PubMed]
26. Dinesh, Y.; Balu, S.K.; Ramalingam, K.; Ramani, P.; Dinesh, Y.; Balu, S.K.; Ramalingam, K.; Ramani, P. Biofabrication and Characterization Using Egg Shell Nanoparticles and Their Haemolytic Analysis: An in-Vitro Study. *Indian J. Pharm. Educ. Res.* **2023**, *57*, s301–s306. [CrossRef]
27. Silva, J.K.D.O.; Bittencourt, C.; Simões, A.Z.; Alves, A.P.R. Determination of the Processing Route for Obtaining Calcium Acetate from Eggshell Waste. *Sustainability* **2026**, *18*, 1448. [CrossRef]
28. Zedda, F.; Atzori, F.; Casu, S.; Sidorowicz, A.; Fais, G.; Desogus, F.; Licheri, R.; Porcu, S.; Cao, G.; Lutzu, G.A.; et al. Green-Synthesized Ag/Zn Nanocomposites from Chlorella Vulgaris Polar Extract: Sustainable Photocatalytic Water Remediation and Kinetic Modeling. *Sustainability* **2026**, *18*, 4607. [CrossRef]
29. Allogmani, A.S.; Mohamed, R.M.; Hasanin, M.S. Green, Eco-Friendly, Highly Biocompatible and Bioactive Nanocomposite-Based Biopolymers Loaded with ZnO@Fe3O4 Nanoparticles. *Polymers* **2023**, *15*, 3641. [CrossRef] [PubMed]
30. López-López, J.R.; Hernández-Chávez, M.A.; López-López, M.d.J.; Tejeda-Ochoa, A.; Cervantes-Gaxiola, M.E.; Parra-Unda, J.R.; Valenzuela-Ramírez, G.G.; Flores-Villaseñor, H.; León-Sicairos, N.; Canizalez-Roman, A.; et al. Tagetes Erecta—Mediated Green Synthesis of ZnO–Ag Nanocomposites: Characterization and Dual Applications in Solar Photocatalytic Degradation and Antibacterial Activity. *Ceramics* **2025**, *8*, 45. [CrossRef]
31. Kusdianto, K.; Puri, N.R.; Shimada, M.; Madhania, S.; Winardi, S. Synergistic Effect of Calcination Temperature and Silver Doping on Photocatalytic Performance of ZnO Material. *Materials* **2025**, *18*, 3362. [CrossRef] [PubMed]
32. Prayitno, B.; Musyarofah, M.; Tajalla, G.U.N.; Nafisah, A.R.; Norhidayah, S.; Kartika, S.A. The effect of calcination temperature and holding time on structural properties of calcia powders derived from eggshell waste. *Indones. Phys. Rev.* **2025**, *8*, 281–299. [CrossRef]
33. Aherkar, V.; Mohammed, A.A.; Al-shimary, A.A.; Ovhal, R.M.; Pawar, S.; Kamble, G.; Ubale, P.A. Synthesis and Characterization of Ag-Doped ZnO Nanostructures and an Assessment on Their Enhanced Bacterial Inhibition and Photocatalytic Degradation. *RSC Adv.* **2026**, *16*, 16253–16263. [CrossRef] [PubMed]
34. Leite, Y.G.d.S.; Nobre, F.X.; Couceiro, P.R.D.C.; Rufino, J.P.F.; Malosso, M.G.; Carvalho, R.P. Production of mixed zeolite using amazonian natural resources and its application in the removal of lead from aqueous solution. *Rev. Geopolít.* **2025**, *16*, e1157. [CrossRef]
35. Hemmami, H.; Zeghoud, S.; Ben Amor, I.; Alnazza Alhamad, A.; Tliba, A.; Alsalme, A.; Cornu, D.; Bechelany, M.; Barhoum, A. Green Synthesis of CaO Nanoparticles from Chicken Eggshells: Antibacterial, Antifungal, and Heavy Metal (Pb2+, Cr2+, Cd2+ and Hg2+) Adsorption Properties. *Front. Environ. Sci.* **2024**, *12*, 1450485. [CrossRef]
36. Thongdamrongtham, S.; Labcom, C.; Saenwang, P.; Chaikhan, S. Waste Shell Valorization for Phosphorus Recovery: Comparative Assessment of Cockle Shell- and Eggshell-Derived Calcium Oxide Adsorbents in Powder and Granular Configurations. *ACS Omega* **2026**, *11*, 34581–34598. [CrossRef] [PubMed]
37. Chuakham, S.; Putkham, A.I.; Chaiyachet, Y.; Saengprajak, A.; Banlue, K.; Tanpaiboonkul, N.; Putkham, A. Scalable Production of Bio-Calcium Oxide via Thermal Decomposition of Solid—Hatchery Waste in a Laboratory-Scale Rotary Kiln. *Sci. Rep.* **2025**, *15*, 865. [CrossRef] [PubMed]
38. Tsai, C.-H.; Morgan, H.M.; Tsai, W.-T. Valorization of Eggshell Powder as a Catalytic Activation Agent for Producing Porous Carbon Materials from Lignocellulosic Waste. *Catalysts* **2025**, *15*, 712. [CrossRef]
39. Wang, Z.; Ma, C.; Harrison, A.; Alsouleman, K.; Gao, M.; Huang, Z.; Chen, Q.; Nie, B. Enhancement Strategies of Calcium Looping Technology and CaO-Based Sorbents for Carbon Capture. *Small* **2025**, *21*, 2412463. [CrossRef] [PubMed]
40. El-Sawaf, A.; Tolan, D.A.; Abdelrahman, M.S.; El-Hay, I.A.; Ismael, M.; Ahmed, A.S.A.; Elshehy, E.A.; Abdu, M.T. Fast In-Situ Synthesis of Mesoporous Prussian Blue-Silica Nanocomposite for Superior Silver Ions Recovery Performance. *J. Chem. Technol. Biotechnol.* **2024**, *99*, 1941–1954. [CrossRef]
41. Pham, H.; Neves, J.C.; Yan, R.; Pankratova, V.; Cao, W.; Zhang, D. Improving Bandgap Determination by Optical Spectroscopy: Comparative Evaluation of ISARS, UV–Vis, and Diffuse Reflectance. *ACS Meas. Sci. Au* **2025**, *5*, 666–676. [CrossRef] [PubMed]

42. Rekha, S.; Sreelakshmi, P.S.; Akhila, V.S.; Amrutha, R.; Anila, E.I. A Study of the Structural, Optical and Antibacterial Properties of Green Synthesized Calcium Oxide Nanoparticles. *Adv. Mater. Lett.* **2024**, *15*, 1749–2402. [CrossRef]
43. Djayasinga, R.; Hadi, S.; Sumardi, S.; Simanjuntak, W.; Sugiarti, M.; Situmeang, R.T.M. Synthesis of Sulfur-Doped Calcium Carbonate Nanocomposite Semiconductor Derived from Chicken Eggshell Powder. In *Proceedings of the 5th International Conference on Applied Sciences, Mathematics, and Informatics (ICASMI 2024)*; Hadi, S., Lumbanraja, F.R., Widiastuti, E.L., Eds.; Advances in Physics Research; Atlantis Press International BV: Dordrecht, The Netherlands, 2025; Volume 13, pp. 163–173. ISBN 978-94-6463-729-8.
44. Sekar, O.; Bincy, F.I.M.; Kim, I.; Dhas, S.A.M.B. Acoustic Shock-Engineered CaO Nanoparticles from Eggshells: Dual Enhancement of Photocatalytic and Antibacterial Properties. *ChemistrySelect* **2025**, *10*, e03601. [CrossRef]
45. Bissenova, M.; Idrissov, N.; Kuspanov, Z.; Umirzakov, A.; Daulbayev, C. Hybrid Adsorption–Photocatalysis Composites: A Sustainable Route for Efficient Water Purification. *Mater. Renew. Sustain. Energy* **2025**, *14*, 44. [CrossRef]
46. Rodiah, S.; Nirwana, R.R.; Erviana, D.; Ariesta, N.; Iskandar, D.; Afriyani, H. Waste-Derived CaO Modified TiO_2 with Reduced Band Gap and Improved Photoresponse under Visible Light. *J. Multidiscip. Appl. Nat. Sci.* **2026**, *6*, 1517–1528. [CrossRef]
47. Kosmulski, M. The pH Dependent Surface Charging and Points of Zero Charge. *X. Update Adv. Colloid Interface Sci.* **2023**, *319*, 102973. [CrossRef] [PubMed]
48. Sukmilin, A.; Pankaew, P.; Chokboribal, J.; Jarusutthirak, C. Degradation of Oxytetracycline in Wastewater by Catalytic Ozonation with Eggshell-Derived Calcium Peroxide. *RSC Adv.* **2025**, *15*, 41209–41218. [CrossRef] [PubMed]
49. Mohsen, D.M.; Al-Jubouri, S.M.; Al-Batty, S. Photocatalytic Degradation of a Cationic Dye Using Ag2O@CuO Nanoellipsoidal Photocatalyst under Ultraviolet Irradiation. *Iraqi J. Chem. Pet. Eng.* **2025**, *26*, 27–40. [CrossRef]
50. Tran, H.D.; Nguyen, D.Q.; Do, P.T.; Tran, U.N.P. Kinetics of Photocatalytic Degradation of Organic Compounds: A Mini-Review and New Approach. *RSC Adv.* **2023**, *13*, 16915–16925. [CrossRef] [PubMed]
51. Minero, C. A Critical Analysis of Kinetic Models in Photocatalysis and Some Necessary Improvements. *Photocatal. Res. Potential* **2025**, *2*, 10020. [CrossRef]
52. Kumar, J.E.; Mulai, T.; Tripathy, A. Behnajady-Modirshahla-Ghanbary Kinetic Model for Degradation of Azo Dye Using Fenton Oxidation Process: A Mini Review. *Next Res.* **2024**, *1*, 100047. [CrossRef]
53. Rawat, M.; Jha, M.K.; Rai, S.K.; Agrawal, P.K. Textile Dye Degradation Technologies with Mechanistic Insights, Kinetic Modeling, and Comparative Performance Analysis. *Discov. Environ.* **2026**, *4*, 508. [CrossRef]
54. Hernández-Orozco, M.M.; Hernández-Rosas, F.; Trinidad-Urbina, R.E.; Ramírez-Bon, R. Induced Hydroxylation on Exfoliated Boron Nitride: Photocatalytic and Adsorptive Properties. *Molecules* **2026**, *31*, 1616. [CrossRef] [PubMed]
55. Rubio-Clemente, A.; Chica, E.; Peñuela, G.A. Optimization Method to Determine the Kinetic Rate Constants for the Removal of Benzo[a]Pyrene and Anthracene in Water through the Fenton Process. *Water* **2022**, *14*, 3381. [CrossRef]
56. Welegergs, G.G.; Gebretinsae, H.G.; Girmay, M.T.; Sindelo, A.; Tedla, A.; Nuru, Z.Y.; Dube, S.; Maaza, M.; Nyokong, T. Plasmonic Silver (Ag) Supported Mesoporous CuO Nanocomposites for Photodegradation of Methylene Blue in Water. *Catal. Lett.* **2025**, *155*, 275. [CrossRef]
57. Ma, D.; Tang, J.; He, G.; Pan, S. Investigation of the Photocatalytic Performance, Mechanism, and Degradation Pathways of Rhodamine B with Bi2O3 Microrods under Visible-Light Irradiation. *Materials* **2024**, *17*, 957. [CrossRef] [PubMed]
58. Yang, X.; Yang, X.; Wu, S. Fabrication of Ag-Doped ZnO Photocatalysts Derived From MIL-125(Zn) With Enhanced Photocatalytic Activity. *Front. Energy Res.* **2022**, *10*, 949551. [CrossRef]
59. Sedefoglu, N. Photocatalytic Performance of Green Synthesized Ag-Doped ZnO Used for Degradation of Hazardous Effluents under Sunlight and UV Light. *Ceram. Int.* **2026**, *52*, 3245–3262. [CrossRef]
60. Li, L.; Wu, G.; Luo, H.; Wang, J.; Wu, H.; Hao, Q.; Han, Y.; Ge, M.; Zhong, C.; Wang, Y. In-Situ Ag Nanoparticle-Embedded Core-Shell Cu-MOFs: Enhanced Photocatalytic Activity for Efficient Degradation of Petroleum Oil Spills in High-Salinity Seawater. *Front. Mar. Sci.* **2026**, *13*, 1787934. [CrossRef]
61. Bhapkar, A.R.; Bhame, S. A Review on ZnO and Its Modifications for Photocatalytic Degradation of Prominent Textile Effluents: Synthesis, Mechanisms, and Future Directions. *J. Environ. Chem. Eng.* **2024**, *12*, 112553. [CrossRef]
62. Tan, S.N.; Yuen, M.L.; Ramli, R.A. Photocatalysis of Dyes: Operational Parameters, Mechanisms, and Degradation Pathway. *Green Anal. Chem.* **2025**, *12*, 100230. [CrossRef]
63. Singh, K.; Maurya, S.; Gupta, S.; Ranjan, N.; Ramanathan, G.; Bhattacharya, S. Effect of the Standardized ZnO/ZnO-GO Filter Element Substrate Driven Advanced Oxidation Process on Textile Industry Effluent Stream: Detailed Analysis of Photocatalytic Degradation Kinetics. *ACS Omega* **2023**, *8*, 28615–28627. [CrossRef] [PubMed]
64. Ranjbari, A.; Adhikary, K.K.; Kashif, M.; Anbari, A.P.; Siddhartha, T.R.; Kim, D.; Yoon, S.; Yoon, J.; Heynderickx, P.M. Comparative Photocatalytic Degradation of Cationic Rhodamine B and Anionic Bromocresol Green Using Reduced ZnO: A Detailed Kinetic Modeling Approach. *Chemosphere* **2025**, *371*, 144052. [CrossRef] [PubMed]

65. Jang, N.; Kim, J.S.; Kim, H.; Kim, D.Y.; Nam, Y.; Han, M.; Kong, S.H. Photocatalytic Degradation of Rhodamine B Using Zinc Oxide/Silver Nanowire Nanocomposite Films under Ultraviolet Irradiation. *R. Soc. Open Sci.* **2025**, *12*, 241967. [CrossRef] [PubMed]
66. Sellam, M.; Azizi, S.; Bouras, D.; Fellah, M.; Obrosov, A.; El-Hiti, G.A. Degradation of Rhodamine B Dye under Visible and Solar Light on Zinc Oxide and Nickel-Doped Zinc Oxide Thin Films. *Opt. Mater.* **2024**, *151*, 115316. [CrossRef]
67. Ahmad, S.; Almehmadi, M.; Janjuhah, H.T.; Kontakiotis, G.; Abdulaziz, O.; Saeed, K.; Ahmad, H.; Allahyani, M.; Aljuaid, A.; Alsaiari, A.A.; et al. The Effect of Mineral Ions Present in Tap Water on Photodegradation of Organic Pollutants: Future Perspectives. *Water* **2023**, *15*, 175. [CrossRef]
68. Kumar, P.; Verma, S.; Kaur, R.; Papac, J.; Kušić, H.; Štangar, U.L. Enhanced Photo-Degradation of N-Methyl-2-Pyrrolidone (NMP): Influence of Matrix Components, Kinetic Study and Artificial Neural Network Modelling. *J. Hazard. Mater.* **2022**, *434*, 128807. [CrossRef] [PubMed]
69. Luo, C.; Wang, S.; Wu, D.; Cheng, X.; Ren, H. UV/Nitrate Photocatalysis for Degradation of Methylene Blue in Wastewater: Kinetics, Transformation Products, and Toxicity Assessment. *Environ. Technol. Innov.* **2022**, *25*, 102198. [CrossRef]
70. Khumphon, J.; Ahmed, R.; Imboon, T.; Giri, J.; Chattham, N.; Mohammad, F.; Kityakarn, S.; Mangala Gowri, V.; Thongmee, S. Boosting Photocatalytic Activity in Rhodamine B Degradation Using Cu-Doped ZnO Nanoflakes. *ACS Omega* **2025**, *10*, 9337–9350. [CrossRef] [PubMed]
71. Jangra, K.; Sharma, A.; Bhardwaj, A.; Garg, S.; Punia, R.; Dahiya, S. Impact of pH Variation and Radical Scavenger on Photocatalytic Dye Degradation of Rhodamine B Dye Using LaAlO3/ZnO Nanocomposites Synthesize by Sol Gel Method. *Mater. Chem. Phys.* **2025**, *334*, 130500. [CrossRef]
72. Sabouri, Z.; Sabouri, S.; Tabrizi Hafez Moghaddas, S.S.; Mostafapour, A.; Amiri, M.S.; Darroudi, M. Facile green synthesis of Ag-doped ZnO/CaO nanocomposites with Caccinia macranthera seed extract and assessment of their cytotoxicity, antibacterial, and photocatalytic activity. *Bioprocess Biosyst. Eng.* **2022**, *45*, 1989–2000. [CrossRef] [PubMed]
73. Thakur, A.S.; Dubey, S.; Vaish, R. Eggshell Waste Derived CaO as a Tribocatalyst for Removal of Rhodamine B Dye under Ambient Light and Sunlight. *Environ. Sci. Pollut. Res.* **2026**, *33*, 1199–1214. [CrossRef] [PubMed]
74. Kumawat, A.; Chhichholiya, S.; Sharma, M.D.; Kumari, P.; Meena, R.K.; Fageria, P. Enhanced visible-light photocatalysis by Au and Ag decorated ZnO for the simultaneous degradation of tetracycline and methylene blue. *Nanoscale Adv.* **2026**, *8*, 1686–1711. [CrossRef] [PubMed]
75. Sistani, P.; Sheikhhosseini, E.; Akhgar, M.R.; Yahyazadehfar, M. Green synthesis of Ag-doped ZnO/CuO nanocomposite using *Sclerorhachis leptoclada* extract and evaluation of its photocatalytic and biological activities. *Chem. Afr.* **2025**, *8*, 1539–1553. [CrossRef]
76. Farrag, A.M.; Awad, M.E.; Aboelnga, M.M.; El-Bindary, A.A. Enhancement of commercial dye photocatalytic degradation through silver-doped kaolinite-zinc oxide quantum dots. *BMC Chem.* **2025**, *19*, 291. [CrossRef] [PubMed]

Disclaimer/Publisher's Note: The statements, opinions and data contained in all publications are solely those of the individual author(s) and contributor(s) and not of MDPI and/or the editor(s). MDPI and/or the editor(s) disclaim responsibility for any injury to people or property resulting from any ideas, methods, instructions or products referred to in the content.